

Volume-averaged nodal projection method for nearly-incompressible elasticity using meshfree and bubble basis functions

A. Ortiz-Bernardin^{a,*}, J. S. Hale^{b,1}, C. J. Cyron^{c,1}

^a*Department of Mechanical Engineering, University of Chile,
Av. Beauchef 850, Santiago 8370448, Chile.*

^b*Faculty of Science, Technology and Communication, University of Luxembourg,
Campus Kirchberg, 6, rue Richard Coudenhove-Kalergi L-1359, Luxembourg.*

^c*Department of Biomedical Engineering, Yale University,
Malone Engineering Center, 55 Prospect Street, New Haven, CT 06511, USA.*

Abstract

We present a displacement-based Galerkin meshfree method for the analysis of nearly-incompressible linear elastic solids, where low-order simplicial tessellations (i.e., 3-node triangular or 4-node tetrahedral meshes) are used as a background structure for numerical integration of the weak form integrals and to get the nodal information for the computation of the meshfree basis functions. In this approach, a volume-averaged nodal projection operator is constructed to project the dilatational strain into an approximation space of equal- or lower-order than the approximation space for the displacement field resulting in a locking-free method. The stability of the method is provided via bubble-like basis functions. Because the notion of an ‘element’ or ‘cell’ is not present in the computation of the meshfree basis functions such low-order tessellations can be used regardless of the order of the approximation spaces desired. First- and second-order meshfree basis functions are chosen as a particular

*Corresponding author. Tel: +56 (2) 297 846 64, Fax: +56 (2) 268 960 57,
Email address: aortizb@ing.uchile.cl (A. Ortiz-Bernardin)

¹These authors contributed equally to this work.

case in the proposed method. Numerical examples are provided in two and three dimensions to demonstrate the robustness of the method, its ability to avoid volumetric locking in the nearly-incompressible regime, and its improved performance when compared to the MINI finite element scheme on the simplicial mesh.

Keywords: meshfree methods, nearly-incompressible elasticity, volumetric locking, projection methods, volume-averaged pressure/strains, bubble functions

1. Introduction

Volumetric locking is a fundamental difficulty that displacement-based Galerkin methods face when dealing with nearly-incompressible solids. Several procedures have been devised to overcome volumetric locking and basically can be grouped in mixed methods and displacement-based methods. Some relevant techniques in mixed methods are mixed variational methods of Simo et al. [1], enhanced assumed strain methods of Simo and Armero [2] and the mixed u - p formulation of Sussman and Bathe [3]. Within displacement-based methods, discontinuous Galerkin finite element methods [4, 5, 6] use independent approximations on different elements and weakly enforce the continuity across boundaries of the elements. Nonconforming finite element methods can also suppress volumetric locking [7, 8, 9]. Another widely used displacement-based finite element method is the so-called B -bar method [10], where the displacement is constructed on a 4-node quadrilateral and the strain is split into its deviatoric and dilatational parts. The volumetric locking is then alleviated by projecting the dilatational strain onto the constant space. A more recent version of the B -bar method that uses higher-order approximations has been proposed for NURBS basis functions [11], where the volumetric locking is alleviated by projecting the dilatational strain onto a space that is one order lower than the displacement space.

Apart from the above methods, there has been a great interest for employing simplicial meshes, particularly in three dimensions, because they facilitate the mesh generation in complex domains. However, low-order triangles/tetrahedra are not appropriate for practical use due to their poor performance in many instances such as bending dominated problems, incompressible media and large deformations. In an effort to cope with their poor performance, various techniques have been developed, which can be classified in four approaches: mixed-enhanced elements [12, 13, 14], pressure stabilization [15, 16, 17], composite pressure fields [18, 19, 20], and average nodal pressure/strains [21, 22, 23, 24, 25, 26, 27, 28]. The last two approaches are displacement-based methods and are broadly based on the idea of reducing pressure (dilatational) constraints to alleviate volumetric locking in low-order meshes. Despite the apparently good performance of the average nodal pressure/strains methods, many of them have been reported to exhibit pressure oscillations and stabilization via bubble functions has been proposed [28]. Recently, nodally integrated continuum elements [29] and subsequent developments that led to patch-averaged assumed strain finite elements [30] were developed based on the assumed-strain [31] concept and low- as well as high-order meshes were considered. Another recent displacement-based approach, which uses bubble functions for pressure stability on simplicial meshes, is the edge-based smoothed finite element method [32].

Displacement-based approaches that are obtained by projection techniques can be viewed within the inf-sup requirements of mixed methods, namely they should satisfy the so-called inf-sup stability condition [33, 34, 35]. Simo and Hughes [31] have established the links between projection (B-bar or assumed strain) methods with mixed methods using the Hu-Washizu variational formulation. In particular, the B-bar method of Refs. [10, 11] can be viewed as a u - p mixed formulation where the pressure variable is hidden in the projected dilatational strain. Therefore, the

projection space should be chosen such that the inf-sup stability condition is satisfied.

In this paper, a displacement-based Galerkin meshfree method is developed for the analysis of nearly-incompressible linear elastic solids, where low-order simplicial tessellations (i.e., 3-node triangular or 4-node tetrahedral meshes) are used as a background structure for numerical integration of the weak form integrals and to get the nodal information for the computation of the meshfree basis functions. The procedure is a projection method designed in the spirit of the B -bar approach. To this end, a projection operator is constructed from the pressure constraint of the u - p mixed formulation, which encompasses the volume-averaged nodal pressure technique of Ortiz et al. [26]. We refer to this operator as the *Volume-Averaged Nodal Projection* (VANP) operator. In the proposed VANP approach we retain the excellent performance of the method of Ortiz et al. [26] for solving the nearly-incompressible elasticity problem on low-order triangular and tetrahedral tessellations. As in the original technique developed in Ref. [26], bubble-like enrichment is essential for stability in the VANP approach.

The advances made in the present paper compared to the method of Ortiz et al. [26] is that it is possible to use higher-order meshfree approximations for the analysis of nearly-incompressible solids using only nodal information from the low-order triangular/tetrahedral tessellations. This extension is non-trivial particularly with respect to ensuring the robust integration of the higher-order meshfree basis functions. First and second-order meshfree approximations are considered to exemplify the VANP approach in this paper.

In the VANP formulation, the numerical integration of the weak form integrals is performed over a background mesh of finite elements. The integration domain is therefore a finite element cell which typically does not coincide with the region that is defined by two overlapping meshfree basis function supports. In addition, meshfree

basis functions are rational (non-polynomial) functions. These are two combined issues that introduce numerical errors when using standard Gauss integration. There have been many efforts to rectify the integration error in meshfree methods. For an early view of the problem the interested reader is referred to the work of Dolbow and Belytschko [36], and for a theoretical background to the work of Babuška and co-workers [37, 38].

In this paper, we are interested in integration schemes that are based on strain smoothing/averaging techniques to alleviate integration errors. Chen et al. [39] proposed a strain correction within the framework of nodal integration techniques that provides patch test satisfaction and significantly reduces integration errors. Ortiz et al. [26] presented a strain correction based on a combined smoothing/averaging procedure for linear approximations on triangular and quadrilateral background meshes and extended these ideas to tetrahedral background meshes in Ref. [40]. Duan et al. [41] proposed a smoothing procedure for second-order approximations on triangular background meshes. Chen et al. [42] proposed a variationally consistent integration method for high-order meshfree approximations that generalizes the notion of nodal integration and is usable for Gauss quadrature on triangles and squares. Recently, Duan et al. [43] used the Hu-Washizu three-field variational principle to demonstrate the variational consistency of the second-order accurate integration scheme for meshfree methods previously presented in Ref. [41] and an extension of this scheme to third-order accuracy is also provided. The corresponding second-order accurate integration scheme for tetrahedral meshes is presented in Duan et al. [44].

The weak form integrals in the VANP formulation are more involved and high-order meshfree basis functions are used. To achieve optimal rates of convergence, it is critical to use the third-order variationally consistent accurate integration rule

of Duan et al. [43]. We use this rule directly for triangular meshes and develop an extension to three dimensions to perform integration on tetrahedral meshes.

The contributions of the VANP method proposed in this paper for the analysis of nearly-incompressible linear elastic solids are listed as follows:

- The projection method developed permits the use of low-order triangular and tetrahedral tessellations irrespective of the desired approximation order. This is not possible in existing finite element displacement-based approaches for nearly-incompressible solids such as nodally-integrated continuum elements [29] and patch-averaged assumed strain elements [30].
- Optimal accuracy in the energy and L^2 norms can be obtained for second order meshfree approximations yet using the nodal positions from low-order triangular/tetrahedral tessellations. To the best of our knowledge, there are no mesh-free or finite element displacement-based methods for nearly-incompressible elasticity exhibiting this feature.
- Smoother pressure fields² can be obtained on low-order triangular/tetrahedral tessellations using first and second order meshfree approximations. This feature is not present in similar methods such as node-based uniform strain elements [22] and meshfree-enriched simplex elements [45] as these methods produce constant strains on the elements.
- In comparing the VANP approach with its finite element counterpart on low-order simplicial tessellations, the MINI element [46], the VANP method delivers more efficient and more accurate solutions with smoother pressure fields.

²Even though the VANP approach is a displacement-based method, the pressure field can be recovered from the computed displacement solution.

The outline of this paper is as follows. Section 2 presents a summary of the maximum-entropy and RPIM basis functions, which are used as particular choices in our meshfree method. The VANP formulation and discrete equations are developed in Section 3. Section 4 is devoted to numerical integration in the VANP method. The performance and accuracy of the VANP formulation are assessed through numerical examples in Section 5. Some concluding remarks are given in Section 6.

2. Meshfree basis functions

For robustness of the VANP formulation, meshfree basis functions that allow direct imposition of essential boundary conditions are considered. In this respect, first- and second-order maximum-entropy (**max-ent**) basis functions [47, 48, 49, 50] are selected since they permit direct imposition of essential boundary conditions at the nodes located on the boundary of a convex domain [48, 50].

Other meshfree basis functions that appear to be usable for direct imposition of essential boundary conditions are RPIM basis functions [51]. Although these functions are known to be incompatible [52], they are endowed with the Kronecker delta property, which only guarantees the vanishing of the interior basis functions at the boundary nodes. According to Ref. [52], this property is sufficient for direct imposition of essential boundary conditions. However, this is not theoretically correct since the Galerkin weak statement demands the vanishing of the interior basis functions not only at the boundary nodes, but also between them (i.e., along the whole boundary). Notwithstanding these theoretical deficiencies, RPIM basis functions have been used many times in Galerkin-based methods [52] with good performance, and so we adopt them as an alternative in the VANP formulation.

2.1. First-order maximum-entropy basis functions

Consider a convex domain represented by a set of n scattered nodes and a prior (weight) function $w_a(\mathbf{x})$ associated with node a . By using the Shannon-Jaynes entropy functional [49], the set of **max-ent** basis functions $\{\phi_a(\mathbf{x}) \geq 0\}_{a=1}^n$ that define the approximation function $\mathbf{u}_h(\mathbf{x}) = \sum_a \phi_a \mathbf{u}_a$ with \mathbf{u}_a the nodal coefficient variables, is obtained via the solution of the following convex optimization problem:

$$\max_{\phi \in \mathbb{R}_+^n} - \sum_{a=1}^n \phi_a(\mathbf{x}) \ln \left(\frac{\phi_a(\mathbf{x})}{w_a(\mathbf{x})} \right) \quad (1a)$$

subject to the linear reproducing conditions:

$$\sum_{a=1}^n \phi_a(\mathbf{x}) = 1 \quad \sum_{a=1}^n \phi_a(\mathbf{x}) \tilde{\mathbf{x}}_a = \mathbf{0}, \quad (1b)$$

where $\tilde{\mathbf{x}}_a = \mathbf{x}_a - \mathbf{x}$ are shifted nodal coordinates and \mathbb{R}_+^n is the non-negative orthant. Typical priors that can be used include kernel or window functions that are well-known in the meshfree literature. In this paper, we use a C^2 quartic polynomial given by

$$w_a(q) = \begin{cases} 1 - 6q^2 + 8q^3 - 3q^4 & 0 \leq q \leq 1 \\ 0 & q > 1 \end{cases}, \quad (2)$$

where $q = \|\mathbf{x}_a - \mathbf{x}\|/\rho_a$ and $\rho_a = \gamma h_a$ is the support radius of the basis function of node a ; γ is a parameter that controls the support-width of the basis function, and h_a is a characteristic nodal spacing associated with node a .

On using Lagrange multipliers, the solution of the variational statement (1) is [49]:

$$\phi_a(\mathbf{x}) = \frac{Z_a(\mathbf{x}; \boldsymbol{\lambda}^*)}{Z(\mathbf{x}; \boldsymbol{\lambda}^*)}, \quad Z_a(\mathbf{x}; \boldsymbol{\lambda}^*) = w_a(\mathbf{x}) \exp(-\boldsymbol{\lambda}^* \cdot \tilde{\mathbf{x}}_a), \quad (3)$$

where $Z(\mathbf{x}; \boldsymbol{\lambda}^*) = \sum_b Z_b(\mathbf{x}; \boldsymbol{\lambda}^*)$, and for instance in three dimensions $\tilde{\mathbf{x}}_a = [\tilde{x}_a \ \tilde{y}_a \ \tilde{z}_a]^T$ and $\boldsymbol{\lambda}^* = [\lambda_1^* \ \lambda_2^* \ \lambda_3^*]^T$. In (3), the Lagrange multiplier vector $\boldsymbol{\lambda}^*$ is the minimizer of

the dual optimization problem:

$$\boldsymbol{\lambda}^* = \arg \min_{\boldsymbol{\lambda} \in \mathbb{R}^d} \ln Z(\mathbf{x}; \boldsymbol{\lambda}), \quad (4)$$

which leads to a system of d nonlinear equations:

$$\mathbf{f}(\boldsymbol{\lambda}) = \nabla_{\boldsymbol{\lambda}} \ln Z(\boldsymbol{\lambda}) = - \sum_a^n \phi_a(\mathbf{x}) \tilde{\mathbf{x}}_a = \mathbf{0}, \quad (5)$$

where d is the order of the spatial dimension of the convex domain and $\nabla_{\boldsymbol{\lambda}}$ stands for the gradient with respect to $\boldsymbol{\lambda}$. Once the converged $\boldsymbol{\lambda}^*$ is found, the basis functions are computed from (3). The gradient of the basis functions is obtained by differentiating (3). The interested reader can find the final expression in [53].

2.2. Second-order maximum-entropy basis functions

Following the discussion in Ref. [50], second-order **max-ent** basis functions are positive and can be defined analogously to the first-order **max-ent** functions on the convex hull of a set of n scattered nodes. To this end, the following optimization problem is solved instead of (1):

$$\max_{\boldsymbol{\phi} \in \mathbb{R}_+^n} - \sum_{a=1}^n \phi_a(\mathbf{x}) \ln(\phi_a(\mathbf{x})) \quad (6a)$$

subject to the quadratic reproducing conditions:

$$\sum_{a=1}^n \phi_a(\mathbf{x}) = 1 \quad \sum_{a=1}^n \phi_a(\mathbf{x}) \tilde{\mathbf{x}}_a = \mathbf{0}, \quad \sum_{a=1}^n \phi_a(\mathbf{x}) \tilde{\mathbf{x}}_a \otimes \tilde{\mathbf{x}}_a = \mathbf{G}(\mathbf{x}), \quad (6b)$$

where \otimes denotes a dyadic product and $\mathbf{G}(\mathbf{x})$ is the so-called gap function, which is required because for $\mathbf{G}(\mathbf{x}) = \mathbf{0}$ the optimization problem (6) can be shown to have no solution except for at the nodes themselves. To overcome this so-called feasibility

problem and obtain yet optimal convergence rates of the resulting approximation scheme, the following gap function was identified in Ref. [50] as a proper choice:

$$\mathbf{G}(\mathbf{x}) = \sum_{a=1}^n \phi_a^{lin}(\mathbf{x}) \mathbf{W}_a \quad (7)$$

with the linear **max-ent** basis functions ϕ_a^{lin} introduced in the previous section and the nodal gap weights being

$$\mathbf{W}_a = \sum_{i=1}^{n_{face}} \alpha \frac{h_a^2}{4} \mathbf{t}_{ai}. \quad (8)$$

Here n_{face} is the dimension of the lowest-dimensional face of the domain to which the node \mathbf{x}_a belongs, h_a is the nodal spacing and \mathbf{t}_{ai} is the i -th unit basis vector of the tangent space to this face. The gap parameter α determines the magnitude of the gap function and is chosen as $\alpha = 4$ [50]. The following semi-analytical solution for the variational statement (6) is obtained using Lagrange multipliers:

$$\phi_a(\mathbf{x}) = \frac{Z_a(\mathbf{x}; \boldsymbol{\lambda}^*; \boldsymbol{\mu}^*)}{Z(\mathbf{x}; \boldsymbol{\lambda}^*; \boldsymbol{\mu}^*)}, \quad Z_a(\mathbf{x}; \boldsymbol{\lambda}^*; \boldsymbol{\mu}^*) = \exp(-\boldsymbol{\lambda}^* \cdot \tilde{\mathbf{x}}_a - \boldsymbol{\mu}^* : [\tilde{\mathbf{x}}_a \otimes \tilde{\mathbf{x}}_a - \mathbf{G}(\mathbf{x})]), \quad (9)$$

where $Z(\mathbf{x}; \boldsymbol{\lambda}^*; \boldsymbol{\mu}^*) = \sum_b Z_b(\mathbf{x}; \boldsymbol{\lambda}^*; \boldsymbol{\mu}^*)$ and the colon denotes a double contraction tensor product; the Lagrange multiplier $\boldsymbol{\lambda}^*$ is the same as the one used in the linear **max-ent**; the additional Lagrange multiplier $\boldsymbol{\mu}^*$ as well as the gap function $\mathbf{G}(\mathbf{x})$ can be written as a symmetric $(d \times d)$ -matrix. The Lagrange multipliers $\boldsymbol{\lambda}^*$ and $\boldsymbol{\mu}^*$ are the minimizers of the dual optimization problem:

$$\{\boldsymbol{\lambda}^*, \boldsymbol{\mu}^*\} = \arg \min_{\boldsymbol{\lambda} \in \mathbb{R}^d, \boldsymbol{\mu} \in \mathbb{R}^{d \times d}} \ln Z(\mathbf{x}; \boldsymbol{\lambda}; \boldsymbol{\mu}), \quad (10)$$

which can be solved similarly to the first-order dual problem (4). The additional Lagrange multiplier $\boldsymbol{\mu}^*$ ensures a rapid Gaussian-like decay of the basis functions around their respective nodes as it does the locality parameter γ for first-order

max-ent functions. As a rule of thumb it can be stated that the effective support of the second-order **max-ent** functions increases with the gap parameter α . For the formulae for the derivatives of the second-order **max-ent** functions the reader is referred to Ref. [50].

2.3. RPIM basis functions

Consider an approximation $\mathbf{u}_h(\mathbf{x})$ of a function $\mathbf{u}(\mathbf{x})$ in an influence domain. The influence domain is defined by the region within a radius ρ from \mathbf{x} and covers a set of N nodes with locations $\{\mathbf{x}_a\}_{a=1}^N$. The Radial Basis Function (RBF) interpolation is defined as [54]:

$$\mathbf{u}_h(\mathbf{x}) = \sum_{a=1}^N c_a \varphi(\|\mathbf{x} - \mathbf{x}_a\|_2), \quad (11)$$

where c_a are coefficients to be found, φ is a radial basis function, and $\|\cdot\|_2$ denotes the Euclidean norm in \mathbb{R}^d . In this work, Buhmann's CSRBFs [55] are used for φ .

In order to construct the RPIM basis functions with a given polynomial consistency, a polynomial extension is added to the RBF [51] so that the approximation is written as

$$u_h(\mathbf{x}) = \sum_{a=1}^N c_a \varphi(\|\mathbf{x} - \mathbf{x}_a\|_2) + \sum_{b=1}^M d_b p_b(\mathbf{x}), \quad (12)$$

where $p_b(\mathbf{x})$ is a monomial of a polynomial of order m with M terms in \mathbf{x} and d_b is a further set of coefficients to be found. The approximation is required to exactly interpolate the function at the nodes giving the condition at every node with location \mathbf{x}_k as follows [54]:

$$\mathbf{u}_h(\mathbf{x}_k) = c_1 \varphi(\|\mathbf{x}_k - \mathbf{x}_1\|_2) + \cdots + c_N \varphi(\|\mathbf{x}_k - \mathbf{x}_N\|_2) = u_k \quad (13)$$

together with

$$\sum_{k=1}^M d_k p_k(\mathbf{x}_k) = 0 \quad (14)$$

to ensure a unique solution [54]. This procedure gives rise to the following system of equations [54]:

$$\begin{bmatrix} \mathbf{A} & \mathbf{P} \\ \mathbf{P}^T & \mathbf{0} \end{bmatrix} \begin{bmatrix} \mathbf{c} \\ \mathbf{d} \end{bmatrix} = \begin{bmatrix} \mathbf{y} \\ \mathbf{0} \end{bmatrix}, \quad (15)$$

where

$$\mathbf{A} = \begin{bmatrix} \varphi(\|\mathbf{x}_1 - \mathbf{x}_1\|) & \dots & \varphi(\|\mathbf{x}_1 - \mathbf{x}_N\|) \\ \vdots & \ddots & \vdots \\ \varphi(\|\mathbf{x}_N - \mathbf{x}_1\|) & \dots & \varphi(\|\mathbf{x}_N - \mathbf{x}_N\|) \end{bmatrix}, \quad \mathbf{P} = \begin{bmatrix} p_1(\mathbf{x}_1) & \dots & p_m(\mathbf{x}_1) \\ \vdots & \ddots & \vdots \\ p_1(\mathbf{x}_N) & \dots & p_m(\mathbf{x}_N) \end{bmatrix}, \quad (16)$$

$$\mathbf{c} = [c_1 \dots c_N]^T, \quad \mathbf{d} = [d_1 \dots d_M]^T, \quad \mathbf{y} = [u_1 \dots u_N]^T. \quad (17)$$

It can be shown that the above system of equations is non-singular and has a unique solution [54]. On defining

$$\mathbf{G} = \begin{bmatrix} \mathbf{A} & \mathbf{P} \\ \mathbf{P}^T & \mathbf{0} \end{bmatrix}, \quad \mathbf{u} = [\mathbf{y} \quad \mathbf{0}]^T, \quad (18)$$

the consistent approximation in matrix form can be written as

$$\mathbf{u}_h(\mathbf{x}) = [\boldsymbol{\varphi}^T(\mathbf{x}) \mathbf{p}^T(\mathbf{x})] \mathbf{G}^{-1} \mathbf{u}. \quad (19)$$

From (19), the basis function row vector is computed as

$$\boldsymbol{\phi}(\mathbf{x}) = [\boldsymbol{\varphi}^T(\mathbf{x}) \mathbf{p}^T(\mathbf{x})] \mathbf{G}^{-1}, \quad (20)$$

where $\boldsymbol{\varphi}(\mathbf{x})^T = [\varphi(\|\mathbf{x} - \mathbf{x}_1\|) \dots \varphi(\|\mathbf{x} - \mathbf{x}_N\|)]$ and $\mathbf{p}(\mathbf{x})^T = [p_1(\mathbf{x}) \dots p_M(\mathbf{x})]$. Finally, the gradient of the basis functions is computed by differentiating (20).

3. Formulation and discrete equations

Consider an elastic body situated in $d = \{2, 3\}$ dimensional space with open domain $\Omega \subset \mathbb{R}^d$ that is bounded by the $d - 1$ dimensional surface Γ whose unit

outward normal is \mathbf{n} . The boundary is assumed to admit decompositions $\Gamma = \Gamma_u \cup \Gamma_t$ and $\emptyset = \Gamma_u \cap \Gamma_t$, where Γ_u is the Dirichlet boundary and Γ_t is the Neumann boundary. The closure of the domain is $\overline{\Omega} \equiv \Omega \cup \Gamma$. The vector $\mathbf{u} : \overline{\Omega} \rightarrow \mathbb{R}^d$ describes the displacement of a point $\mathbf{x} \in \overline{\Omega}$ of the elastic body when the body is subjected to external tractions $\hat{\mathbf{t}} : \Gamma_t \rightarrow \mathbb{R}^d$ and body forces $\mathbf{b} : \Omega \rightarrow \mathbb{R}^d$. The Dirichlet (essential) boundary conditions are $\hat{\mathbf{u}} : \Gamma_u \rightarrow \mathbb{R}^d$.

The kinematic relation between the small strain tensor $\boldsymbol{\varepsilon}$ and the displacement vector \mathbf{u} is:

$$\boldsymbol{\varepsilon} = \nabla_s \mathbf{u} = \frac{1}{2} (\nabla \mathbf{u} + (\nabla \mathbf{u})^T). \quad (21)$$

The elastic body is assumed to be homogeneous and isotropic allowing the stress $\boldsymbol{\sigma}$ to be related to the strain $\boldsymbol{\varepsilon}$ by

$$\boldsymbol{\sigma}(\boldsymbol{\varepsilon}) = 2\mu\boldsymbol{\varepsilon} + \lambda \operatorname{tr} \boldsymbol{\varepsilon} \mathbf{I} = 2\mu \nabla_s \mathbf{u} + \lambda (\nabla \cdot \mathbf{u}) \mathbf{I}, \quad (22)$$

where λ and μ are the Lamé's first and second parameters, respectively. These parameters are related to the Young's modulus E and Poisson's ratio ν by

$$\lambda = \frac{E\nu}{(1+\nu)(1-2\nu)}, \quad (23a)$$

$$\mu = \frac{E}{2(1+\nu)}. \quad (23b)$$

The elastic body becomes nearly-incompressible when $\nu \rightarrow 1/2$, which results in the following divergence-free (or incompressibility) constraint to be satisfied by the displacement field:

$$\nabla \cdot \mathbf{u} = \operatorname{tr} \boldsymbol{\varepsilon} = \varepsilon_{kk} = \varepsilon^{\operatorname{vol}} \approx 0, \quad (24)$$

which can be used to approximate the hydrostatic pressure field $p : \overline{\Omega} \rightarrow \mathbb{R}$ as [56]

$$p = -\lambda \nabla \cdot \mathbf{u} = -\lambda \operatorname{tr} \boldsymbol{\varepsilon} = -\lambda \varepsilon_{kk} = -\lambda \varepsilon^{\operatorname{vol}}. \quad (25)$$

Typically, when placed under such a strong constraint the numerical solution via displacement-based weak formulation cannot describe movement whilst satisfying (24); thus volumetric locking occurs. The volumetric locking can be suppressed using the u - p mixed formulation, which includes the effect of the divergence-free constraint (24).

3.1. u - p mixed weak form

Let $\mathcal{U} := \{\mathbf{u} : \mathbf{u} \in H^1(\Omega), \mathbf{u} = \hat{\mathbf{u}} \text{ on } \Gamma_u\}$ and $\mathcal{V} := \{\delta\mathbf{u} : \delta\mathbf{u} \in H^1(\Omega), \delta\mathbf{u} = \mathbf{0} \text{ on } \Gamma_u\}$ be the trial and test spaces for the displacement field, respectively. Since the pressure is unique only up to a constant, we define $\mathcal{P} := \{p : p \in L^2(\Omega), \int_{\Omega} p \, d\Omega = 0\}$ and let $p \in \mathcal{P}$ and $\delta p \in \mathcal{P}$ be the trial and test functions for the pressure variable, respectively. By substituting (25) into (22), the stress tensor can be rewritten as

$$\boldsymbol{\sigma}(\boldsymbol{\varepsilon}) = -p\mathbf{I} + 2\mu\nabla_s\mathbf{u}. \quad (26)$$

Using the foregoing definitions, the u - p mixed weak form reads [56]:

Problem 1. Find $\mathbf{u} \in \mathcal{U}$ and $p \in \mathcal{P}$ such that

$$\begin{aligned} 2\mu \int_{\Omega} \nabla_s \mathbf{u} : \nabla_s \delta\mathbf{u} \, d\Omega - \int_{\Omega} p \nabla \cdot \delta\mathbf{u} \, d\Omega \\ = \int_{\Omega} \mathbf{b} \cdot \delta\mathbf{u} \, d\Omega + \int_{\Gamma_t} \hat{\mathbf{t}} \cdot \delta\mathbf{u} \, d\Gamma \quad \forall \delta\mathbf{u} \in \mathcal{V}, \end{aligned} \quad (27a)$$

$$\int_{\Omega} \delta p \left(\nabla \cdot \mathbf{u} + \frac{p}{\lambda} \right) \, d\Omega = 0 \quad \forall \delta p \in \mathcal{P}. \quad (27b)$$

In the discrete equivalent of (27), solutions $\mathbf{u}_h \in \mathcal{U}_h \subset \mathcal{U}$ and $p_h \in \mathcal{P}_h \subset \mathcal{P}$ are sought. In addition, the pair (\mathbf{u}_h, p_h) should satisfy a uniform inf-sup condition that is independent of the discretization size and λ to ensure stability and convergence [34, 35, 33].

3.2. Modified displacement-based weak form

An alternative locking-free approach, where the only variable is the displacement field, can be obtained using the additive decomposition of the deformation strain into its deviatoric and dilatational parts, and projecting the latter into another space. This is the approach used by Elguedj et al. [11] and has the good feature that yields a symmetric tangent stiffness matrix when the approach is extended to nonlinear elasticity. The VANP formulation is also based on this approach.

The additive decomposition of the discrete strain is:

$$\begin{aligned}
\boldsymbol{\varepsilon}_h(\mathbf{u}_h) &= \underbrace{\boldsymbol{\varepsilon}_h(\mathbf{u}_h) - \frac{1}{3} \operatorname{tr} \boldsymbol{\varepsilon}_h(\mathbf{u}_h) \mathbf{I}}_{\text{deviatoric}} + \underbrace{\frac{1}{3} \operatorname{tr} \boldsymbol{\varepsilon}_h(\mathbf{u}_h) \mathbf{I}}_{\text{dilatational}} \\
&= \left(1 - \frac{1}{3} \operatorname{tr}\right) \boldsymbol{\varepsilon}_h(\mathbf{u}_h) \mathbf{I} + \frac{1}{3} \operatorname{tr} \boldsymbol{\varepsilon}_h(\mathbf{u}_h) \mathbf{I} \\
&= \left(1 - \frac{1}{3} \operatorname{tr}\right) \boldsymbol{\varepsilon}_h(\mathbf{u}_h) \mathbf{I} + \frac{1}{3} \boldsymbol{\varepsilon}_h^{\text{vol}}(\mathbf{u}_h) \mathbf{I} \\
&= \boldsymbol{\varepsilon}_h^{\text{dev}}(\mathbf{u}_h) + \boldsymbol{\varepsilon}_h^{\text{dil}}(\mathbf{u}_h), \tag{28}
\end{aligned}$$

which is used to define a discrete modified strain denoted by $\bar{\boldsymbol{\varepsilon}}_h(\mathbf{u}_h)$, where the bar indicates the application of a projection operator π_h on its unmodified dilatational part, i.e.

$$\bar{\boldsymbol{\varepsilon}}_h(\mathbf{u}_h) = \boldsymbol{\varepsilon}_h^{\text{dev}}(\mathbf{u}_h) + \pi_h [\boldsymbol{\varepsilon}_h^{\text{dil}}(\mathbf{u}_h)] = \boldsymbol{\varepsilon}_h^{\text{dev}}(\mathbf{u}_h) + \bar{\boldsymbol{\varepsilon}}_h^{\text{dil}}(\mathbf{u}_h). \tag{29}$$

The projection operator in (29) has not been applied to the deviatoric part since the dilatational part is the responsible for the volumetric locking. The modified dilatational strain is to be understood as an improved strain that precludes volumetric locking. A modified potential energy functional will be defined using (29).

Problem 2. *The displacement $\mathbf{u}_h \in \mathcal{U}_h \subset \mathcal{U}$ can be found as the unique minimum point of the modified potential energy functional $\bar{\Pi}$:*

$$\bar{\Pi}(\mathbf{u}_h) = \inf_{\mathbf{u}_h} \int_{\Omega} \psi[\bar{\boldsymbol{\varepsilon}}_h(\mathbf{u}_h)] d\Omega - \int_{\Omega} \mathbf{b} \cdot \mathbf{u}_h d\Omega - \int_{\Gamma_t} \hat{\mathbf{t}} \cdot \mathbf{u}_h d\Gamma. \tag{30}$$

On taking the first variation of the modified functional leads to the following general modified discrete weak form:

Problem 3. Find the displacement $\mathbf{u}_h \in \mathcal{U}_h \subset \mathcal{U}$ such that

$$\begin{aligned} \int_{\Omega} \bar{\boldsymbol{\sigma}}_h(\bar{\boldsymbol{\varepsilon}}_h(\mathbf{u}_h)) : \bar{\boldsymbol{\varepsilon}}_h(\delta \mathbf{u}_h) \, d\Omega \\ = \int_{\Omega} \mathbf{b} \cdot \delta \mathbf{u}_h \, d\Omega + \int_{\Gamma_t} \hat{\mathbf{t}} \cdot \delta \mathbf{u}_h \, d\Gamma \quad \forall \delta \mathbf{u}_h \in \mathcal{V}_h \subset \mathcal{V}. \end{aligned} \quad (31)$$

By means of (22) and (28), the modified stress in (31) becomes:

$$\bar{\boldsymbol{\sigma}}_h = 2\mu \boldsymbol{\varepsilon}_h + \lambda \bar{\boldsymbol{\varepsilon}}_h^{\text{vol}} \mathbf{I}. \quad (32)$$

By substituting (29) and (32) into (31) yields the following modified discrete weak form for nearly-incompressible linear elastostatics:

Problem 4. Find the displacement $\mathbf{u}_h \in \mathcal{U}_h \subset \mathcal{U}$ such that

$$\begin{aligned} \int_{\Omega} [2\mu \boldsymbol{\varepsilon}_h(\mathbf{u}_h) + \lambda \bar{\boldsymbol{\varepsilon}}_h^{\text{vol}}(\mathbf{u}_h) \mathbf{I}] : \left[\left(1 - \frac{1}{3} \text{tr} \boldsymbol{\varepsilon}_h(\delta \mathbf{u}_h) \mathbf{I} + \frac{1}{3} \bar{\boldsymbol{\varepsilon}}_h^{\text{vol}}(\delta \mathbf{u}_h) \mathbf{I} \right) \right] \, d\Omega \\ = \int_{\Omega} \mathbf{b} \cdot \delta \mathbf{u}_h \, d\Omega + \int_{\Gamma_t} \hat{\mathbf{t}} \cdot \delta \mathbf{u}_h \, d\Gamma \quad \forall \delta \mathbf{u}_h \in \mathcal{V}_h \subset \mathcal{V}. \end{aligned} \quad (33)$$

The final step is the construction of an appropriate operator π_h that defines the ‘barred’ quantities in (33) such that volumetric locking is alleviated. In brief, the idea is to find such an operator from the pressure constraint (27b). This adopts the form of an L^2 projection. To this end, (27b) can be rearranged and later solved for p_h to arrive at the following expression:

$$\begin{aligned} p_h &= -\lambda \pi_h(\boldsymbol{\nabla} \cdot \mathbf{u}_h) = -\lambda \pi_h(\text{tr} \boldsymbol{\varepsilon}_h(\mathbf{u}_h)) \\ &= -\lambda \text{tr} \pi_h(\boldsymbol{\varepsilon}_h(\mathbf{u}_h)) = -\lambda \text{tr} \bar{\boldsymbol{\varepsilon}}_h(\mathbf{u}_h) = -\lambda \bar{\boldsymbol{\varepsilon}}_h^{\text{vol}}(\mathbf{u}_h). \end{aligned} \quad (34)$$

If an expression like (34) is available, the pressure can be eliminated from the formulation making the system uniquely determined by the displacement field; furthermore, the space \mathcal{P}_h becomes a function of the space \mathcal{U}_h , namely $\mathcal{P}_h(\mathcal{U}_h)$.

3.3. Volume-averaged nodal projection operator

The explicit form of the projection operator is derived from the volume-averaged nodal pressure technique introduced in the work of Ortiz et al. [26]. To this end, let the domain tessellation with simplices be denoted by $\mathcal{T}(\Omega)$. The tessellation consists of 3-node triangular or 4-node tetrahedral cells denoted by \mathcal{C} . The vertices of the tessellation, denoted by $\mathcal{V}(\mathcal{T})$, are then used to define the standard node set \mathcal{N}^s . In addition to the standard node set, we define a barycenter node set as \mathcal{N}^b with nodes located at the barycenter of each cell \mathcal{C} in the tessellation $\mathcal{T}(\Omega)$. So, an enhanced node set is defined as $\mathcal{N}^+ = \mathcal{N}^s \cup \mathcal{N}^b$. Fig. 1 depicts a schematic representation of a two-dimensional simplicial tessellation used in the VANP method.

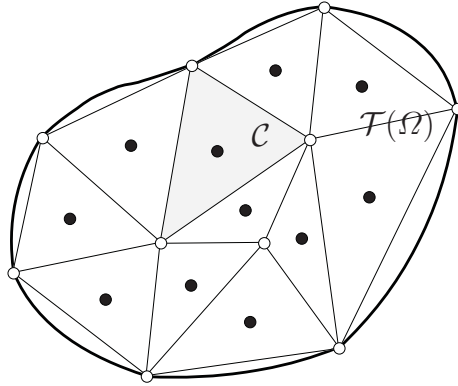


Fig. 1: Schematic representation of a two-dimensional simplicial tessellation for the VANP method.

In our approach, the simplicial tessellation $\mathcal{T}(\Omega)$ that connects the standard node set \mathcal{N}^s is generated using a meshing software and the Gauss points locations are computed based on this mesh. The enhanced node set \mathcal{N}^+ is constructed when needed by adding the extra required nodes to the standard node set \mathcal{N}^s . This poses no problem or additional complexity in the method since the flexibility of meshfree methods permits the addition of nodes to the simplicial mesh very easily.

To obtain the projection operator, the pressure constraint (27b) is discretized using

$$p_h(\mathbf{x}) = \sum_{b=1}^n \phi_b(\mathbf{x}) p_b, \quad (35a)$$

$$\delta p_h(\mathbf{x}) = \sum_{c=1}^n \phi_c(\mathbf{x}) \delta p_c, \quad (35b)$$

where n is the number of nodes in the node set \mathcal{N}^s , whose associated meshfree basis functions ϕ_i ($i = b, c$) have a nonzero discrete value at the sampling point of Cartesian coordinate \mathbf{x} . If Gauss integration is used, the coordinates of the sampling point are the Cartesian coordinates of a given Gauss point. By substituting (35) into the pressure constraint (27b), it can be shown that after relying on the arbitrariness of nodal pressure test functions and performing row-sum on the discrete pressure term leads to the following *volume-averaged nodal pressure* [26]:

$$p_c = -\lambda \frac{\int_{\Omega_c} \phi_c(\mathbf{x}) \nabla \cdot \mathbf{u}_h d\Omega}{\int_{\Omega_c} \phi_c(\mathbf{x}) d\Omega} = -\lambda \frac{\int_{\Omega_c} \phi_c(\mathbf{x}) \boldsymbol{\varepsilon}_h^{\text{vol}} d\Omega}{\int_{\Omega_c} \phi_c(\mathbf{x}) d\Omega}, \quad (36)$$

where the integration volume Ω has been replaced with Ω_c to indicate that due to the row-sum procedure the integration volume is the union of cells that are attached to node c associated with the pressure degree of freedom p_c (see Fig. 2). Eq. (36) gives rise to the VANP operator as

$$\pi_c[\cdot] = \frac{\int_{\Omega_c} \phi_c(\mathbf{x}) [\cdot] d\Omega}{\int_{\Omega_c} \phi_c(\mathbf{x}) d\Omega}, \quad (37)$$

As can be inferred from (36), the nodal operator applied to $\boldsymbol{\varepsilon}_h^{\text{vol}}$ gives its nodal representation as

$$\boldsymbol{\varepsilon}_c^{\text{vol}} = \pi_c[\boldsymbol{\varepsilon}_h^{\text{vol}}] = \frac{\int_{\Omega_c} \phi_c(\mathbf{x}) [\boldsymbol{\varepsilon}_h^{\text{vol}}] d\Omega}{\int_{\Omega_c} \phi_c(\mathbf{x}) d\Omega}. \quad (38)$$

Finally, by the linear combination $p_h = \sum_c \phi_c p_c$, the bar operator is given by the following projection operator:

$$\pi[\cdot] = \sum_{c=1}^n \phi_c(\mathbf{x}) \pi_c[\cdot] = \sum_{c=1}^n \phi_c(\mathbf{x}) \left\{ \frac{\int_{\Omega_c} \phi_c(\mathbf{x}) [\cdot] d\Omega}{\int_{\Omega_c} \phi_c(\mathbf{x}) d\Omega} \right\}. \quad (39)$$

Thus, $\bar{\boldsymbol{\varepsilon}}_h^{\text{vol}}$ is computed as follows:

$$\bar{\boldsymbol{\varepsilon}}_h^{\text{vol}} = \pi[\boldsymbol{\varepsilon}_h^{\text{vol}}] = \sum_{c=1}^n \phi_c(\mathbf{x}) \pi_c[\boldsymbol{\varepsilon}_h^{\text{vol}}] = \sum_{c=1}^n \phi_c(\mathbf{x}) \left\{ \frac{\int_{\Omega_c} \phi_c(\mathbf{x}) \boldsymbol{\varepsilon}_h^{\text{vol}} d\Omega}{\int_{\Omega_c} \phi_c(\mathbf{x}) d\Omega} \right\} = \sum_{c=1}^n \phi_c(\mathbf{x}) \boldsymbol{\varepsilon}_c^{\text{vol}}. \quad (40)$$

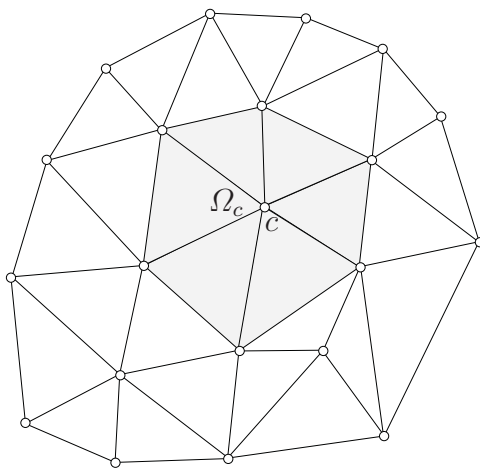


Fig. 2: Schematic representation of an integration volume for the computation of the VANP operator associated with node c .

Because the VANP method has its roots in the u - p mixed formulation, it is important to consider the inf-sup stability [33, 34, 35]. However, inf-sup stability is difficult to prove in meshfree methods. Therefore, we do not provide an analytical proof for the inf-sup condition, but rather we mimic well-known inf-sup stable finite element schemes. To this end, first-order meshfree basis functions are used to construct the space \mathcal{U}_h with the enhanced node set \mathcal{N}^+ and the space $\mathcal{P}_h(\mathcal{U}_h)$ with the standard node set \mathcal{N}^s . This mimics the inf-sup stable MINI finite element [46]. For high-order

approximations, two inf-sup stable finite elements are considered: the second-order conforming Crouzeix & Raviart element [57] and the Taylor-Hood element [58]. The former is mimicked using second-order meshfree basis functions to construct the space \mathcal{U}_h with the enhanced node set \mathcal{N}^+ and first-order meshfree basis functions to construct the space $\mathcal{P}_h(\mathcal{U}_h)$ with the standard node set \mathcal{N}^s . The Taylor-Hood element is mimicked using second-order meshfree basis functions to construct the space \mathcal{U}_h and first-order meshfree basis to construct the space $\mathcal{P}_h(\mathcal{U}_h)$ both with the standard node set \mathcal{N}^s . It is stressed that this is done only for stability purposes. Ultimately, it is our interest to compare the VANP approach with the MINI element because both use the same tessellation.

For implementation purposes of the VANP operator, it should be noted that the use of the aforementioned meshfree discretizations for construction of \mathcal{U}_h and $\mathcal{P}_h(\mathcal{U}_h)$ spaces imply that the basis functions that appear in the operator (39) are computed using the standard node set \mathcal{N}^s , but $\varepsilon_h^{\text{vol}}$ in (40) using either the enhanced node set \mathcal{N}^+ or the standard node set \mathcal{N}^s depending on whether bubble enrichment is used or not, respectively, since $\varepsilon_h^{\text{vol}}$ is computed from the displacement field.

3.4. Discrete equations

The discrete modified weak form is obtained by introducing the following approximations into (33):

$$\mathbf{u}_h(\mathbf{x}) = \sum_{a=1}^n \phi_a(\mathbf{x}) \mathbf{u}_a, \quad (41a)$$

$$\delta \mathbf{u}_h(\mathbf{x}) = \sum_{b=1}^n \phi_b(\mathbf{x}) \delta \mathbf{u}_b, \quad (41b)$$

where $\phi_a(\mathbf{x})$ and $\phi_b(\mathbf{x})$ are meshfree basis functions. Thus, the corresponding discrete strains that appear in the modified weak form (33) (in Voigt notation) become

$$\boldsymbol{\varepsilon}_h(\mathbf{u}_h) = \sum_{a=1}^n \mathbf{B}_a(\mathbf{x}) \mathbf{u}_a, \quad (42)$$

$$\boldsymbol{\varepsilon}_h(\delta \mathbf{u}_h) = \sum_{b=1}^n \mathbf{B}_b(\mathbf{x}) \delta \mathbf{u}_b, \quad (43)$$

$$\bar{\boldsymbol{\varepsilon}}_h^{\text{vol}}(\mathbf{u}_h) = \sum_{c=1}^n \phi_c(\mathbf{x}) \pi_c \left[\mathbf{m}^T \sum_{a=1}^n \mathbf{B}_a \right] \mathbf{u}_a, \quad (44)$$

$$\bar{\boldsymbol{\varepsilon}}_h^{\text{vol}}(\delta \mathbf{u}_h) = \sum_{c=1}^n \phi_c(\mathbf{x}) \pi_c \left[\mathbf{m}^T \sum_{b=1}^n \mathbf{B}_b \right] \delta \mathbf{u}_b, \quad (45)$$

where in two dimensions

$$\mathbf{m} = \begin{bmatrix} 1 & 1 & 0 \end{bmatrix}^T, \quad (46)$$

$$\mathbf{B}_a = \begin{bmatrix} \phi_{a,x} & 0 \\ 0 & \phi_{a,y} \\ \phi_{a,y} & \phi_{a,x} \end{bmatrix}, \quad (47)$$

and in three dimensions

$$\mathbf{m} = \begin{bmatrix} 1 & 1 & 1 & 0 & 0 & 0 \end{bmatrix}^T, \quad (48)$$

$$\mathbf{B}_a = \begin{bmatrix} \phi_{a,x} & 0 & 0 \\ 0 & \phi_{a,y} & 0 \\ 0 & 0 & \phi_{a,z} \\ \phi_{a,y} & \phi_{a,x} & 0 \\ \phi_{a,z} & 0 & \phi_{a,x} \\ 0 & \phi_{a,z} & \phi_{a,y} \end{bmatrix}. \quad (49)$$

Finally, on collecting all these discrete quantities and replacing them into the modified weak form (33), and appealing to the arbitrariness of nodal variations leads to the following system of equations:

$$(\mathbf{K}^1 + \mathbf{K}^2 + \mathbf{K}^3 + \mathbf{K}^4) \mathbf{u} = \mathbf{f}, \quad (50a)$$

where \mathbf{u} is the column vector of nodal coefficients and

$$\mathbf{K}_{ab}^1 = \int_{\Omega} \mathbf{B}_a^T \mathbf{l}_{\text{dev}}^T \mathbf{C}_{\mu} \mathbf{B}_b d\Omega, \quad (50b)$$

$$\mathbf{K}_{ab}^2 = \lambda \int_{\Omega} \mathbf{B}_a^T \mathbf{l}_{\text{dev}}^T \mathbf{m} \sum_{c=1}^n \phi_c \pi_c [\mathbf{m}^T \mathbf{B}_b] d\Omega, \quad (50c)$$

$$\mathbf{K}_{ab}^3 = \frac{1}{3} \int_{\Omega} \left(\mathbf{m} \sum_{c=1}^n \phi_c \pi_c [\mathbf{m}^T \mathbf{B}_a] \right)^T \mathbf{C}_{\mu} \mathbf{B}_b d\Omega, \quad (50d)$$

$$\mathbf{K}_{ab}^4 = \frac{\lambda}{3} \int_{\Omega} \left(\mathbf{m} \sum_{c=1}^n \phi_c \pi_c [\mathbf{m}^T \mathbf{B}_a] \right)^T \mathbf{m} \sum_{c=1}^n \phi_c \pi_c [\mathbf{m}^T \mathbf{B}_b] d\Omega, \quad (50e)$$

$$\mathbf{f}_a = \int_{\Omega} \phi_a \mathbf{b} d\Omega + \int_{\Gamma_t} \phi_a \hat{\mathbf{t}} d\Gamma \quad (50f)$$

with the following matrices due to the Voigt notation:

$$\mathbf{l}_{\text{dev}} = \mathbf{l} - \frac{1}{3} \mathbf{m} \mathbf{m}^T \quad (\mathbf{l} \text{ is the identity matrix}), \quad (50g)$$

and the material matrix being

$$\mathbf{C}_{\mu} = \begin{bmatrix} 2\mu & 0 & 0 \\ 0 & 2\mu & 0 \\ 0 & 0 & \mu \end{bmatrix} \quad (50h)$$

in two dimensions, or

$$\mathbf{C}_\mu = \begin{bmatrix} 2\mu & 0 & 0 & 0 & 0 & 0 \\ 0 & 2\mu & 0 & 0 & 0 & 0 \\ 0 & 0 & 2\mu & 0 & 0 & 0 \\ 0 & 0 & 0 & \mu & 0 & 0 \\ 0 & 0 & 0 & 0 & \mu & 0 \\ 0 & 0 & 0 & 0 & 0 & \mu \end{bmatrix} \quad (50i)$$

in three dimensions. Once the nodal coefficients are obtained from (50a), the nodal displacement at node i of Cartesian coordinates \mathbf{x}_i is computed by evaluating (41a) at $\mathbf{x} = \mathbf{x}_i$.

4. Numerical integration

The cell-based integration of discrete quantities that depend on basis functions derivatives introduces integration errors when standard Gauss integration is used. To alleviate these integration errors in the VAMP method, a special procedure is performed to correct the values of the nodal basis functions derivatives at the Gauss points.

A strain correction technique that alleviates integration errors in meshfree methods, ensures patch test satisfaction to machine precision and converges optimally for first-order meshfree approximations, was developed in Ref. [26]. In the present paper, second-order **max-ent** basis functions and second-order **RPIM** basis functions are used. Particularly, the derivatives of the latter ones are much more complicated than the derivatives of the former ones. Thus, the first-order correction presented in Ref. [26] is not sufficiently accurate for integration of the weak form integrals. As a remedy, the third-order variationally consistent accurate integration scheme

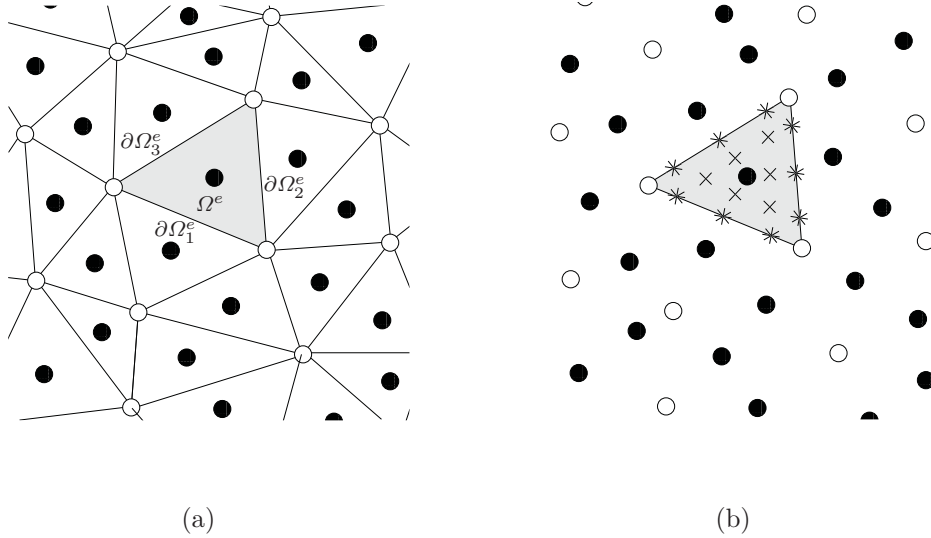


Fig. 3: Geometric entities for the third-order accurate integration scheme. (a) Simplicial tessellation, where the shaded region represents an integration cell whose domain is denoted by Ω^e and its boundary by $\partial\Omega^e = \partial\Omega_1^e \cup \partial\Omega_2^e \cup \partial\Omega_3^e$; and (b) the integration cell and nodes, where the interior Gauss points are depicted as + and the boundary Gauss points as *. Note that depending on the support size of the nodal basis functions, nodes that are beyond the cell can contribute at a Gauss point if their basis functions take a nonzero value at that point.

presented in Ref. [43] is adopted to correct the nodal basis functions derivatives on triangular meshes and we extend this rule to tetrahedral meshes.

The third-order integration scheme needs an integration cell that is obtained from a simplicial tessellation. Fig. 3 depicts a typical tessellation and a representative integration cell in two dimensions for this scheme; the enhanced node set \mathcal{N}^+ is also shown to remark that the nodal basis functions derivatives are to be computed using the enhanced node set since they stem from the displacement field.

The third-order accurate integration scheme for correction of nodal basis functions derivatives follows. For simplicity, the derivations are given in detail only for two-

dimensions. The Cartesian coordinate system is chosen, where for convenience $x \equiv x_1$ and $y \equiv x_2$. In addition, n_j ($j = 1, 2$) is the j -th component of the unit outward normal to a cell edge in the Cartesian coordinate system.

For the cubic approximation basis

$$\mathbf{p}(\mathbf{x}) = [1 \ x_1 \ x_2 \ x_1x_1 \ x_1x_2 \ x_2x_2 \ x_1x_1x_1 \ x_1x_1x_2 \ x_1x_2x_2 \ x_2x_2x_2]^T, \quad (51)$$

the corresponding stress field is quadratic. That is, the stress can be represented using a quadratic basis as

$$\sigma_{ij} = a_0 + a_1x_1 + a_2x_2 + a_3x_1x_1 + a_4x_1x_2 + a_5x_2x_2. \quad (52)$$

Hence, the quadratic basis is

$$f(\mathbf{x}) = [1 \ x_1 \ x_2 \ x_1x_1 \ x_1x_2 \ x_2x_2]^T, \quad (53)$$

whose derivative (δ_{ij} is the Kronecker delta symbol) is

$$f_{,j}(\mathbf{x}) = [0 \ \delta_{1j} \ \delta_{2j} \ 2x_1\delta_{1j} \ x_2\delta_{1j} + x_1\delta_{2j} \ 2x_2\delta_{2j}]^T, \quad (54)$$

The corrected nodal derivatives (see Eq. (35) in Ref. [43]) can be expressed as

$$\int_{\Omega^e} \phi_{a,j} f(\mathbf{x}) d\Omega^e = \int_{\Gamma^e} \phi_a f(\mathbf{x}) n_j d\Gamma^e - \int_{\Omega^e} \phi_a f_{,j}(\mathbf{x}) d\Omega^e, \quad (55)$$

leading to the following integration constraints that are to be met by the meshfree

basis functions derivatives:

$$\int_{\Omega^e} \phi_{a,1} d\Omega^e = \int_{\Gamma^e} \phi_a n_1 d\Gamma^e, \quad (56a)$$

$$\int_{\Omega^e} \phi_{a,1} x_1 d\Omega^e = \int_{\Gamma^e} \phi_a x_1 n_1 d\Gamma^e - \int_{\Omega^e} \phi_a d\Omega^e, \quad (56b)$$

$$\int_{\Omega^e} \phi_{a,1} x_2 d\Omega^e = \int_{\Gamma^e} \phi_a x_2 n_1 d\Gamma^e, \quad (56c)$$

$$\int_{\Omega^e} \phi_{a,1} x_1 x_1 d\Omega^e = \int_{\Gamma^e} \phi_a x_1 x_1 n_1 d\Gamma^e - \int_{\Omega^e} \phi_a 2x_1 d\Omega^e, \quad (56d)$$

$$\int_{\Omega^e} \phi_{a,1} x_1 x_2 d\Omega^e = \int_{\Gamma^e} \phi_a x_1 x_2 n_1 d\Gamma^e - \int_{\Omega^e} \phi_a x_2 d\Omega^e, \quad (56e)$$

$$\int_{\Omega^e} \phi_{a,1} x_2 x_2 d\Omega^e = \int_{\Gamma^e} \phi_a x_2 x_2 n_1 d\Gamma^e \quad (56f)$$

for $\phi_{a,1}$, and

$$\int_{\Omega^e} \phi_{a,2} d\Omega^e = \int_{\Gamma^e} \phi_a n_2 d\Gamma^e, \quad (56g)$$

$$\int_{\Omega^e} \phi_{a,2} x_1 d\Omega^e = \int_{\Gamma^e} \phi_a x_1 n_2 d\Gamma^e, \quad (56h)$$

$$\int_{\Omega^e} \phi_{a,2} x_2 d\Omega^e = \int_{\Gamma^e} \phi_a x_2 n_2 d\Gamma^e - \int_{\Omega^e} \phi_a d\Omega^e, \quad (56i)$$

$$\int_{\Omega^e} \phi_{a,2} x_1 x_1 d\Omega^e = \int_{\Gamma^e} \phi_a x_1 x_1 n_2 d\Gamma^e, \quad (56j)$$

$$\int_{\Omega^e} \phi_{a,2} x_1 x_2 d\Omega^e = \int_{\Gamma^e} \phi_a x_1 x_2 n_2 d\Gamma^e - \int_{\Omega^e} \phi_a x_1 d\Omega^e, \quad (56k)$$

$$\int_{\Omega^e} \phi_{a,2} x_2 x_2 d\Omega^e = \int_{\Gamma^e} \phi_a x_2 x_2 n_2 d\Gamma^e - \int_{\Omega^e} \phi_a 2x_2 d\Omega^e \quad (56l)$$

for $\phi_{a,2}$.

The integration constraints (56) are solved using Gauss integration on the integration cell shown in Fig. 3(b), which leads to the following system of linear equations:

$$\mathbf{Q}d_j = \mathbf{f}_j, \quad j = 1, 2 \quad (57a)$$

where \mathbf{Q} and \mathbf{f}_j are given in Ref. [43] (see Eq. (42) therein), and the j -th corrected basis function derivative at the six interior Gauss points of coordinates \mathbf{x}_i ($i = 1, 2, \dots, 6$) is given by the solution vector

$$\mathbf{d}_j = \left[\phi_{a,j}(\mathbf{x}_1) \quad \phi_{a,j}(\mathbf{x}_2) \quad \phi_{a,j}(\mathbf{x}_3) \quad \phi_{a,j}(\mathbf{x}_4) \quad \phi_{a,j}(\mathbf{x}_5) \quad \phi_{a,j}(\mathbf{x}_6) \right]^T. \quad (57b)$$

In the preceding equations, the index a runs through the combined nodal contribution³ that results from the union of nodal contributions corresponding to each of the interior and edge Gauss points in the cell.

The corrected derivatives given in (57b) are used to define the deformation matrix (Eq. (47) or (49)) that appears in the stiffness matrices of the VANP method.

Finally, in three dimensions the integration cell is a tetrahedron and the integration constraints can be derived from the quadratic basis

$$f(\mathbf{x}) = [1 \quad x_1 \quad x_2 \quad x_3 \quad x_1x_1 \quad x_2x_2 \quad x_3x_3 \quad x_1x_2 \quad x_1x_3 \quad x_2x_3]^T, \quad (58)$$

and its derivative

$$f_{,j}(\mathbf{x}) = [0 \quad \delta_{1j} \quad \delta_{2j} \quad \delta_{3j} \quad 2x_1\delta_{1j} \quad 2x_2\delta_{2j} \quad 2x_3\delta_{3j} \quad x_2\delta_{1j}+x_1\delta_{2j} \quad x_3\delta_{1j}+x_1\delta_{3j} \quad x_3\delta_{2j}+x_2\delta_{3j}]^T. \quad (59)$$

The third-order integration scheme has not been developed for tetrahedral cells in Ref [43]. Therefore, the quadratures that are needed for tetrahedral cells are given in Appendix A.

5. Numerical examples

In this section, the performance and accuracy of the VANP formulation are assessed via numerical examples. The following notation is adopted for presenting the VANP

³The nodal contribution at a given Gauss point of coordinate \mathbf{x} is defined as the indices of the nodes whose basis functions have a nonzero value at \mathbf{x} .

results: VANP- T_p^a/T_q -b, where T_p is the approximation space of polynomial order p for the displacement field and T_q is the approximation space of polynomial order q in which the dilatational strain is projected; the superscript a is set as follows: $a = +$ when bubble enrichment is specified (\mathcal{N}^+ is the node set used) or it is removed in case bubble enrichment is not considered (\mathcal{N}^s is the node set used); and b stands for the type of meshfree basis function that is used for the approximation spaces. Thus, b = m is used for **max-ent** basis functions, whereas b = r for **RPIM** basis functions. By using the preceding definitions the following VANP schemes are considered: VANP- T_1^+/T_1 -m, VANP- T_2^+/T_1 -m, VANP- T_2^+/T_1 -r, VANP- T_2/T_1 -m, VANP- T_2/T_1 -r.

In all the VANP computations, the third-order variationally consistent accurate integration scheme detailed in Section 4 is used and the nodal pressure is obtained from the computed nodal coefficients using (36). The base background mesh, which only contains the node set \mathcal{N}^s , is generated using a meshing software. The enhanced node set \mathcal{N}^+ is constructed when needed by adding the extra required nodes to the standard node set \mathcal{N}^s .

5.1. Cantilever beam

To show the accuracy and convergence of the VANP method in nearly-incompressible elasticity, a cantilever beam of unit thickness with a parabolic end load P is considered. Fig. 4 presents the geometry of the beam. A regular background mesh of 3-node triangles with a mesh pattern of $2n$ divisions along the length of the beam and n divisions along the height of the beam is chosen for the definition of node set \mathcal{N}^s . The coarsest mesh is obtained with $n = 4$. The essential boundary conditions on the clamped edge are applied according to the analytical solution given by Timoshenko

and Goodier [59]:

$$u_x = -\frac{Py}{6\bar{E}I} \left((6L - 3x)x + (2 + \bar{\nu})y^2 - \frac{3D^2}{2}(1 + \bar{\nu}) \right), \quad (60a)$$

$$u_y = \frac{P}{6\bar{E}I} (3\bar{\nu}y^2(L - x) + (3L - x)x^2), \quad (60b)$$

where $\bar{E} = E/(1 - \nu^2)$ with the Young's modulus set to $E = 210000$ MPa and $\bar{\nu} = \nu/(1 - \nu)$ with the Poisson's ratio set to $\nu = 0.4999$; $L = 200$ mm is the length of the beam, $D = 100$ mm is the height of the beam, and I the second-area moment of the beam section. The total load on the traction boundary is $P = -5000$ N.

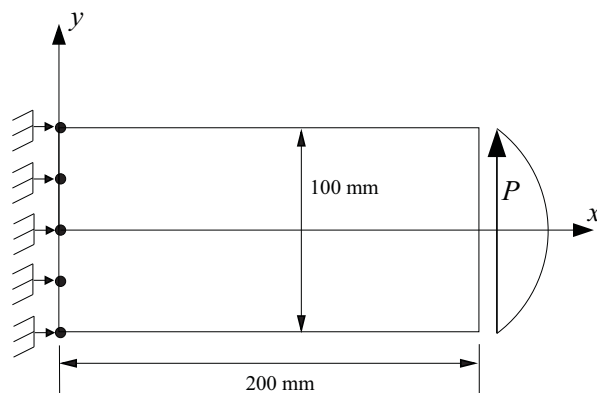


Fig. 4: Cantilever beam problem. Model geometry and boundary conditions

The convergence rates in the energy and L^2 norms of the error are depicted in Fig. 5. In the convergence plots, the nodal spacing is set to the length of the element side and denoted by h . The convergence rates in the energy norm of the error are presented in Fig. 5(a). The optimal convergence rates in the energy norm of the error are 1 for linear displacements and 2 for quadratic displacements [56]. From Fig. 5(a), it is observed that both the MINI element and VANP- T_1^+/T_1 -m schemes deliver the optimal rate of convergence, but the latter is more accurate than the former. With respect to the second-order maxent approaches, the VANP- T_2^+/T_1 -m

scheme delivers the optimal convergence rate, whereas the VANP- T_2/T_1 -m slightly loses the optimal convergence due to the absence of bubble enrichment. On the other hand, the second-order RPIM schemes, VANP- T_2^+/T_1 -r and VANP- T_2/T_1 -r, only exhibit linear convergence.

The convergence rates in the L^2 -norm of the error are shown in Fig. 5(b). The optimal convergence rates in the L^2 -norm of the error are 2 for linear displacements and 3 for quadratic displacements [56]. Once again, both the MINI element and the VANP- T_1^+/T_1 -m schemes deliver the optimal rate of convergence, but the latter is more accurate than the former; all the second-order VANP approaches exhibit the optimal rate of convergence in the L^2 -norm of the error.

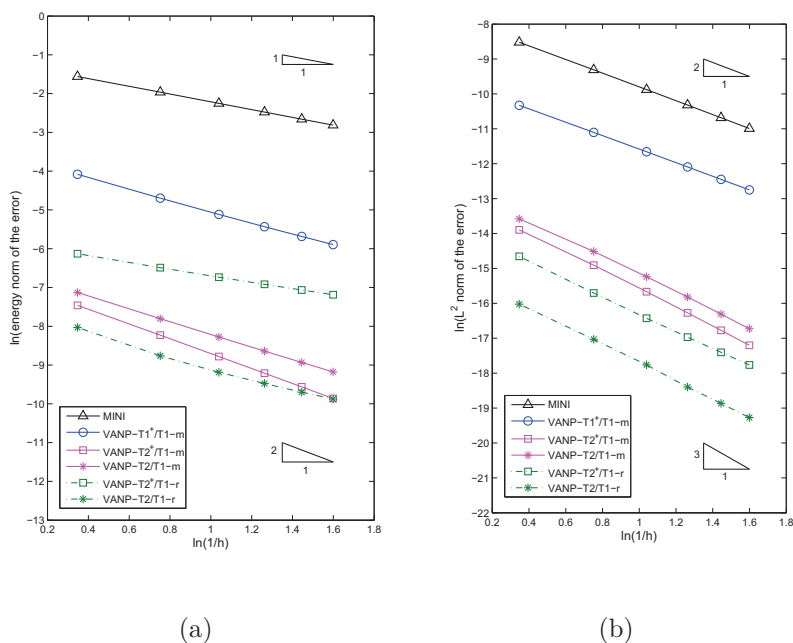


Fig. 5: Convergence study for the cantilever beam problem. (a) Energy norm of the error and (b) L^2 norm of the error.

Finally, the computational efficiency of the different approaches is studied. In

order to compare the first with second order methods, the energy and L^2 norms of the errors of the first order methods were computed with more refined meshes to obtain accuracies comparable to the accuracies of the second order methods; and to compare the VANP formulation with the MINI element, only the bubble-enriched VANP methods are considered. The computational efficiency of the different approaches is presented in Fig. 6. All the VANP methods are more efficient than the MINI element in both the energy and L^2 norms of the error when a certain level of accuracy is desired, particularly, as the mesh is refined.

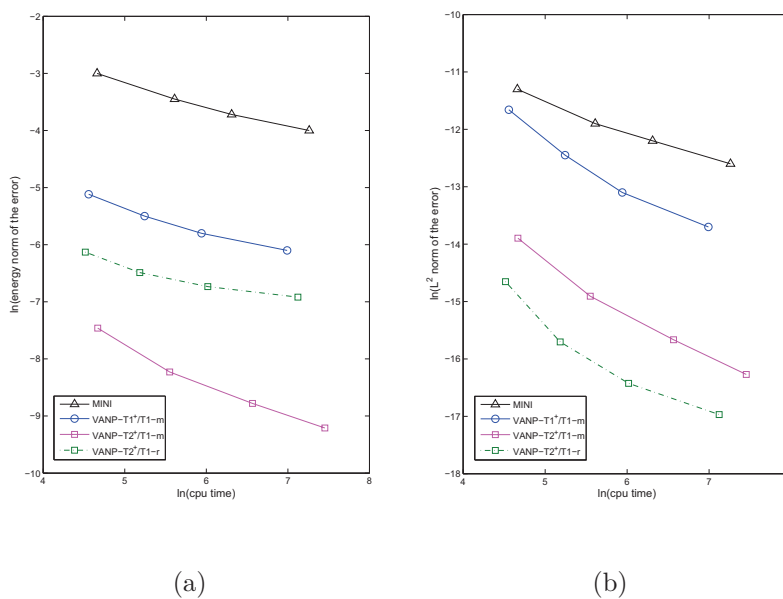


Fig. 6: Computational efficiency for the cantilever beam problem. (a) Energy norm of the error and (b) L^2 norm of the error.

5.2. Cook's Membrane

The membrane shown in Fig. 7(a) is used to test the behavior of the VANP formulation under combined bending and shear (see for instance, Refs. [60, 18, 11] for

previous use of this standard benchmark test). The left edge is clamped and the right end is subjected to a uniformly distributed shear load of $P = 6.25$ N/mm (total shear load of 100 N). The following material parameters are set: $E = 240.565$ MPa and $\nu = 0.4999$. A regular background mesh of 3-node triangles with a mesh pattern of $n \times n$ divisions per side is chosen for the definition of node set \mathcal{N}^s . A reference mesh for $n = 20$ is shown in Fig. 7(b). The unstructured background mesh depicted in Fig. 7(c) is also considered for some tests.

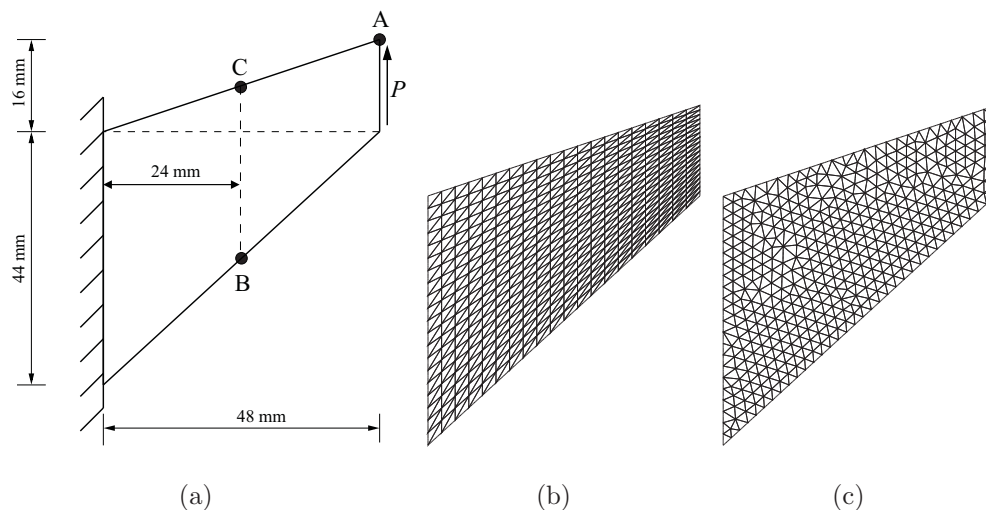


Fig. 7: Cook's membrane problem. (a) Model geometry and boundary conditions; (b) sample regular background mesh; and (c) unstructured background mesh.

A first study is devoted to the convergence of the vertical tip displacement at point A upon mesh refinement. The results are summarized in Fig. 8. The numerical results reveal that the VANP approaches deliver better convergence than the MINI element and that VANP- T_1^+/T_{1-m} and VANP- T_2^+/T_{1-r} are in good agreement between them and both converge to the reference value (around 8 mm) obtained from Ref. [11]. The scheme without bubbles VANP- T_2/T_{1-r} also exhibits good convergence to the

reference value, although slightly inferior to the convergence of the former VANP cases.

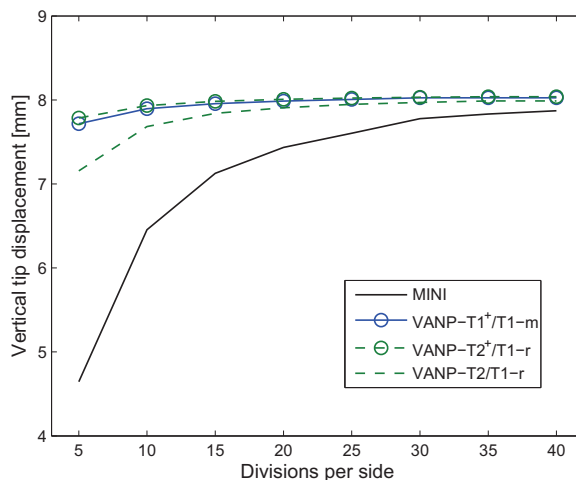


Fig. 8: Cook’s membrane problem. Convergence of the vertical tip displacement.

A second study is performed to show the smoothness of the nodal pressure delivered by the VANP formulation. Here, the nodal pressure is measured along the line BC (see Fig. 7(a)) using the structured mesh shown in Fig. 7(b). The results are depicted in Fig. 9. It is observed that the MINI element exhibits small pressure oscillations near the starting and ending points on the line BC, whereas the VANP- $T_1^+/T_1\text{-m}$ scheme delivers smooth pressure along the whole line. The VANP- $T_2^+/T_1\text{-r}$ approach also delivers smooth pressure along the whole line. However, the VANP- $T_2/T_1\text{-r}$ scheme, which has no bubble enrichment, presents severe pressure oscillations. Finally, the nodal pressure is computed using the unstructured mesh depicted in Fig. 7(c). The pressure smoothness delivered by the VANP formulation is readily evident in the pictorial shown in Fig. 10, where only the VANP- $T_2/T_1\text{-r}$ scheme exhibits pressure oscillations due to the absence of bubble enrichment.

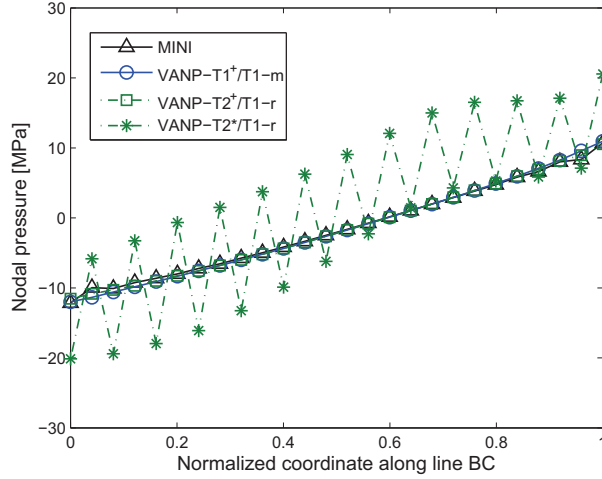


Fig. 9: Cook's membrane problem. Nodal pressure along the line BC .

5.3. Plane strain compression of a constrained block

This compression problem is used to evaluate the VANP formulation in a highly constrained setting in two dimensions. Similar benchmark problems are found in Refs. [18, 61, 62]. As shown in Fig. 11(a), a square block of dimensions 1×1 mm and unit thickness is fully constrained on its Dirichlet boundary (bottom, left, and right edges). A downward traction of 4000 N/mm is applied over the center portion of the top edge covering 1/3 of the edge's length. The following material parameters are specified: $E = 210000$ MPa and $\nu = 0.4999$. Plane strain condition is assumed. A reference background mesh of 3-node triangles for the definition of the node set \mathcal{N}^s is shown in Fig. 11(b) for a regular tessellation and in Fig. 11(c) for an unstructured one. In this example, the non-bubble-enriched schemes are not shown since they produce highly oscillatory pressure fields and therefore are not stable. This lack of stability has already been demonstrated in the previous examples.

The compression level is defined as the ratio of the absolute value of the vertical

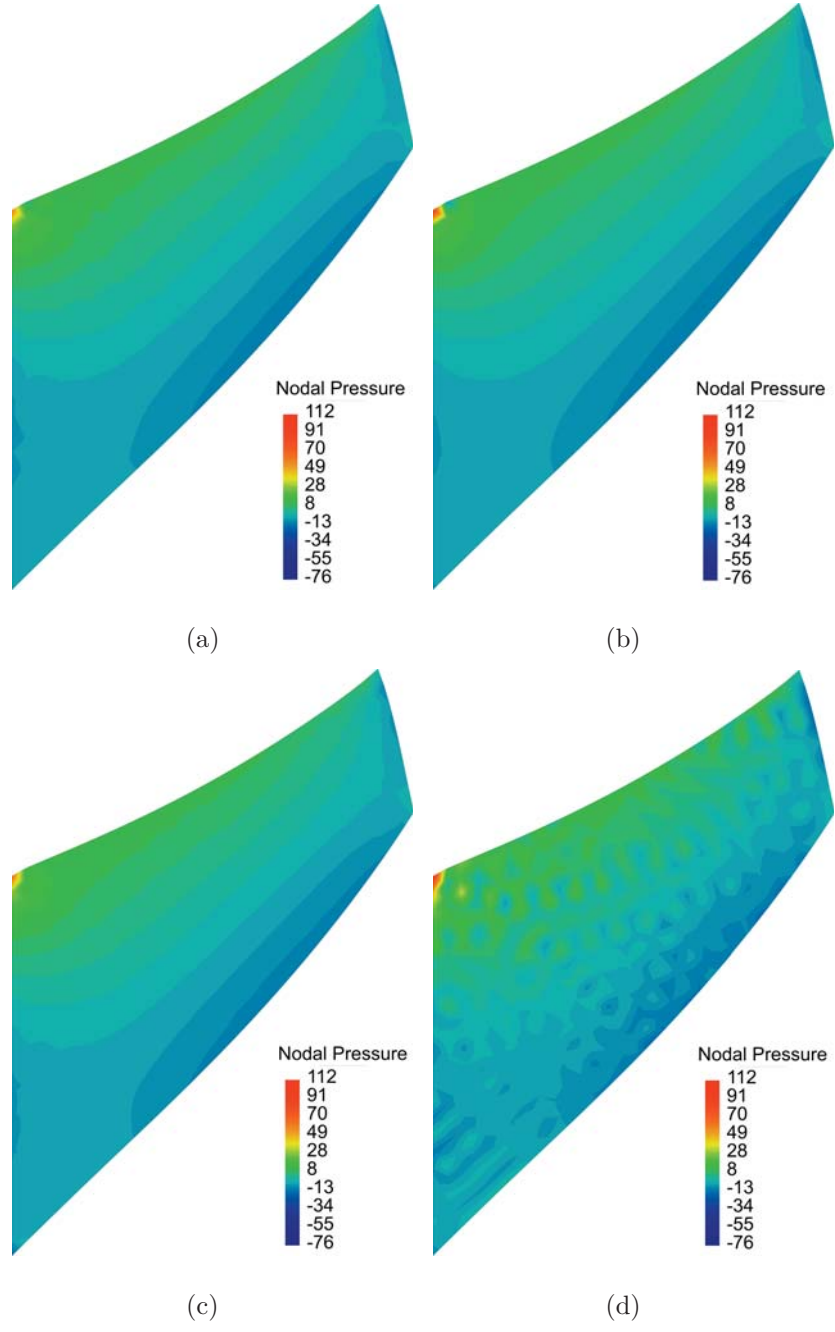


Fig. 10: Cook’s membrane problem. Nodal pressure variable on the unstructured background mesh for (a) MINI element, (b) $\text{VANP-}T_1^+/T_1\text{-m}$, (c) $\text{VANP-}T_2^+/T_1\text{-r}$, and (d) $\text{VANP-}T_2/T_1\text{-r}$.

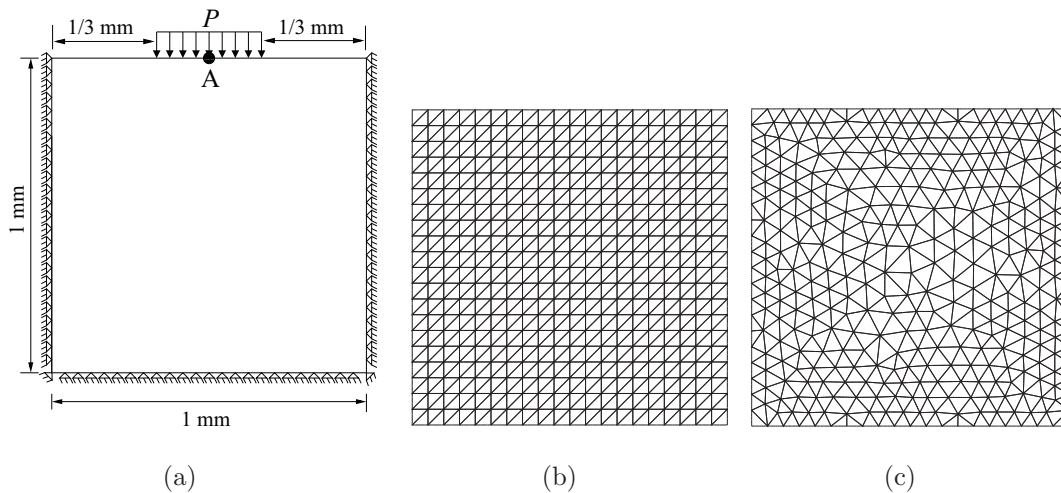


Fig. 11: Plane strain compression of a constrained block. (a) Model geometry and boundary conditions; (b) sample regular background mesh; and (c) unstructured background mesh.

displacement at point A to the height of the block. In the first test, the convergence of the compression level upon mesh refinement of the regular mesh is studied. The results for the MINI element and first- and second-order VAMP schemes are presented in Fig. 12. All the schemes show convergence as the mesh is refined. However, the MINI element scheme presents a slower convergence.

The second test is devoted to study the smoothness of the nodal pressure variable. For this purpose the unstructured mesh shown in Fig. 11(c) is considered. The nodal pressures are shown in Fig. 13. It is observed that the nodal pressure is reasonable smooth for the MINI element formulation (Fig. 13(a)); however, the first-order `max-ent` VAMP scheme presents even smoother pressure fields (Fig. 13(b)). Smooth pressure is also obtained for the second-order enriched VAMP schemes (Figs. 13(c) and 13(d)).

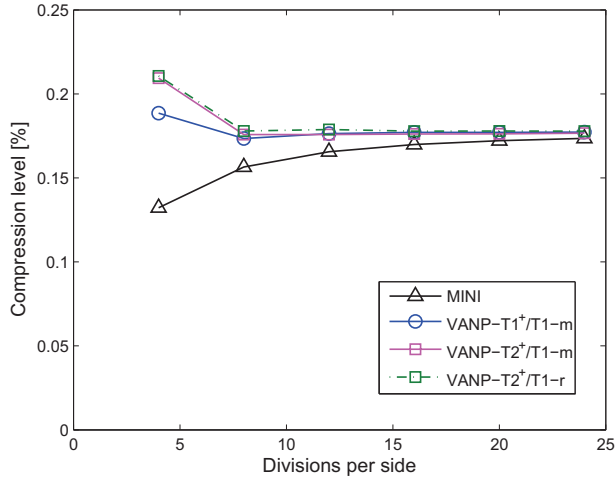


Fig. 12: Plane strain compression of a constrained block. Convergence of the compression level at point A.

5.4. Compression of a constrained block

Finally, a three-dimensional highly constrained problem is considered. A rectangular block of dimensions $1 \times 0.5 \times 0.5$ mm is constrained as shown in Fig. 14(a). The downward traction is 1000 MPa. The following material parameters are set: $E = 210000$ MPa and $\nu = 0.4999$. For the construction of the node set \mathcal{N}^s , the faces of the rectangular domain are divided as follows: $2n$ divisions along the length, n divisions along the height, and n divisions along the depth. A regular background mesh of 4-node tetrahedra is generated to define the node set \mathcal{N}^s . A sample mesh for $n = 6$ is shown in Fig. 14(b).

The compression level is defined as the ratio of the absolute value of the vertical displacement on edge AB to the height of the block. The convergence of the compression level upon mesh refinement is presented in Fig. 15. In this particular example, the MINI element converges and performs as good as the **max-ent** VANP schemes. Although the VANP- T_2^+/T_1 -r scheme shows a tendency to converge, it

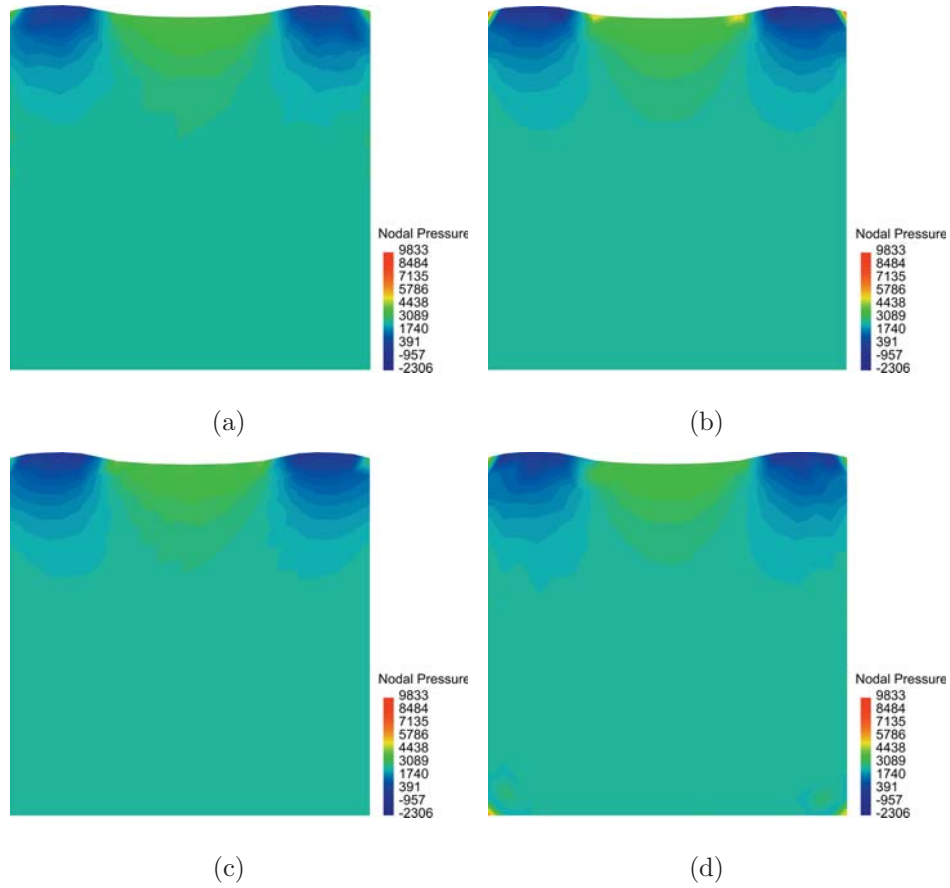


Fig. 13: Plane strain compression of a constrained block. Nodal pressure variable for (a) MINI element, (b) VANP- T_1^+/T_1 -m, (c) VANP- T_2^+/T_1 -m, and (d) VANP- T_2^+/T_1 -r. In these plots the unstructured background mesh depicted in Fig. 11(c) is used.

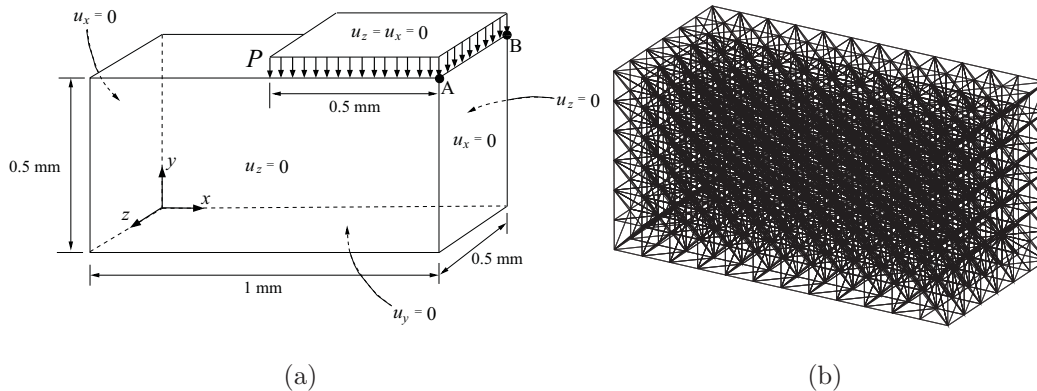


Fig. 14: Compression of a constrained block. (a) Model geometry and boundary conditions, and (b) sample background mesh.

does it significantly slower than the rest of the schemes.

With respect to the smoothness of the nodal pressure variable, Fig. 16 reveals that the MINI element presents small pressure oscillations. In contrast, the VANP- T_1^+/T_1 -m and VANP- T_2^+/T_1 -m schemes present smooth pressure fields. On the other hand, the pressure field for the VANP- T_2^+/T_1 -r scheme behaves oscillatory.

6. Conclusions

In this paper, a high-order displacement-based Galerkin meshfree method has been proposed for the analysis of nearly-incompressible linear elastic solids using the nodal information from low-order triangular/tetrahedral tessellations. In this procedure, a projection operator is constructed from the pressure constraint of the u - p mixed formulation and used to project the dilatational strain onto an approximation space of equal- or lower-order than the approximation space for the displacement field. The stability of the method is provided via bubble-like functions, which requires the addition of an interior node to every cell in the simplicial tessellation. This, however, is a straight-forward task due to the flexibility offered by meshfree methods.

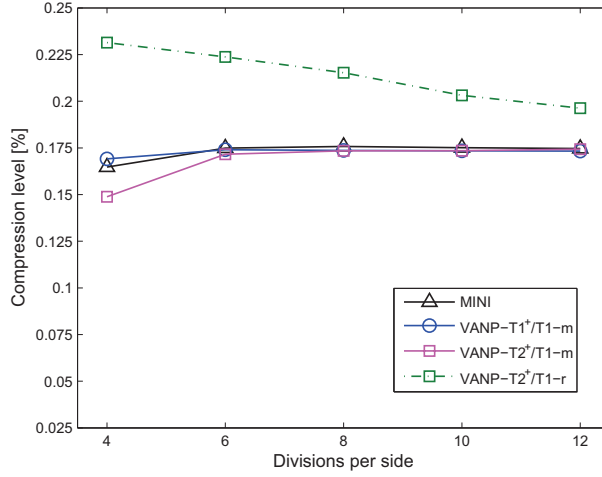


Fig. 15: Compression of a constrained block. Convergence of the compression level on edge AB .

First and second order both **max-ent** and RPIM basis functions were considered as particular cases to exemplify the VANP formulation. The low-order tessellation is also used to numerically integrate the VANP weak form integrals. For accuracy purposes, the third-order variationally consistent accurate integration rule of Duan et al. [43] was adopted for triangular meshes and an extension of this rule to three dimensions was developed for integration on tetrahedral meshes.

The performance of the VANP formulation was assessed through several examples in two and three dimensions. The results showed that the method is devoid of volumetric locking and that the enrichment of the displacement field with bubble-like nodes is fundamental to obtain smooth nodal pressures from the computed displacement field. The rates of convergence in the energy and L^2 -norm of the error were found to be optimal in first and second order **max-ent** VANP schemes, whereas second-order RPIM VANP schemes converged optimally in the L^2 -norm and only linearly in the energy norm. In comparing the VANP approach with its finite element counter-

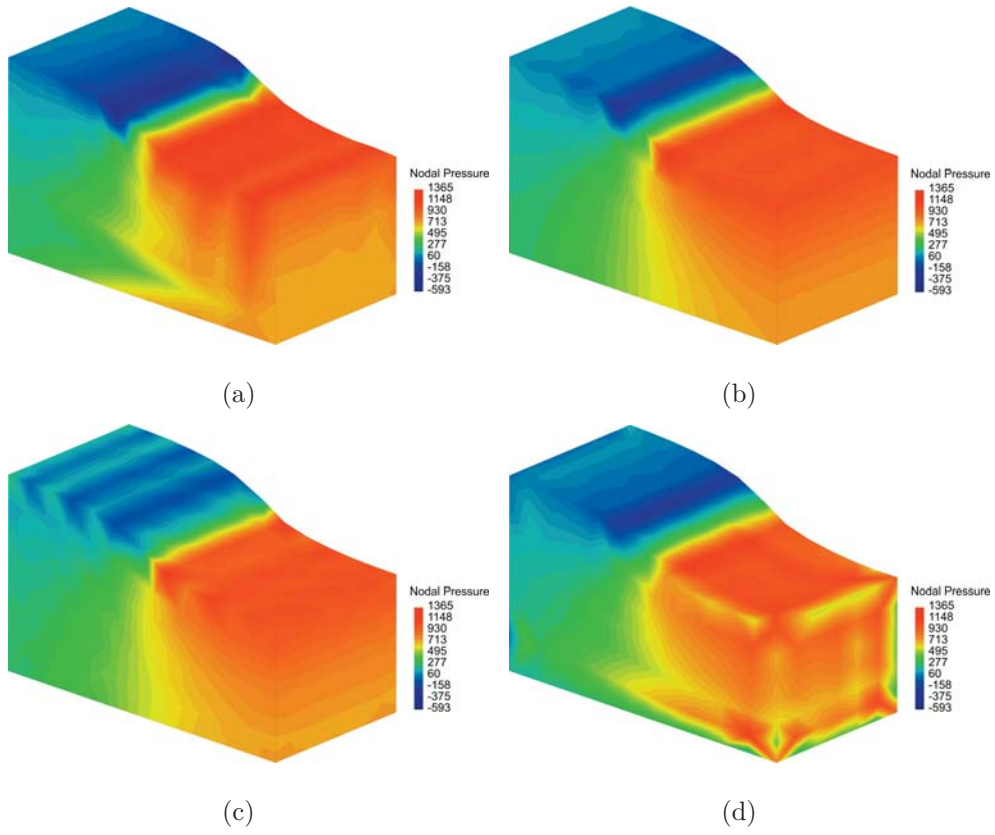


Fig. 16: Compression of a constrained block. Nodal pressure variable for (a) MINI element, (b) VANP- T_1^+/T_1 -m, (c) VANP- T_2^+/T_1 -m, and (d) VANP- T_2^+/T_1 -r.

part, the MINI element [46], it can be stated that the VANP approach provides greater efficiency, greater accuracy and better convergence properties on low-order simplicial tessellations. An extension of the VANP formulation to nonlinear regime is currently under investigation.

Appendix A. Quadratures for the tetrahedral cell

The quadratures given here ensure invertibility of Q in (57). For a tetrahedral cell, the following 10-point rule is used for the interior Gauss points:

$$T = \begin{bmatrix} 0.7784952948213300 & 0.0738349017262234 & 0.0738349017262234 & 0.0738349017262234 \\ 0.0738349017262234 & 0.7784952948213300 & 0.0738349017262234 & 0.0738349017262234 \\ 0.0738349017262234 & 0.0738349017262234 & 0.7784952948213300 & 0.0738349017262234 \\ 0.0738349017262234 & 0.0738349017262234 & 0.0738349017262234 & 0.7784952948213300 \\ 0.4062443438840510 & 0.4062443438840510 & 0.0937556561159491 & 0.0937556561159491 \\ 0.4062443438840510 & 0.0937556561159491 & 0.4062443438840510 & 0.0937556561159491 \\ 0.4062443438840510 & 0.0937556561159491 & 0.0937556561159491 & 0.4062443438840510 \\ 0.0937556561159491 & 0.4062443438840510 & 0.4062443438840510 & 0.0937556561159491 \\ 0.0937556561159491 & 0.4062443438840510 & 0.0937556561159491 & 0.4062443438840510 \\ 0.0937556561159491 & 0.0937556561159491 & 0.4062443438840510 & 0.4062443438840510 \end{bmatrix} \quad (\text{A.1})$$

as the tetrahedral coordinates, and

$$\mathbf{w} = \begin{bmatrix} 0.0476331348432089 \\ 0.0476331348432089 \\ 0.0476331348432089 \\ 0.0476331348432089 \\ 0.1349112434378610 \\ 0.1349112434378610 \\ 0.1349112434378610 \\ 0.1349112434378610 \\ 0.1349112434378610 \\ 0.1349112434378610 \\ 0.1349112434378610 \end{bmatrix} \quad (\text{A.2})$$

as the corresponding weights; whereas the following 6-point rule is used for the face Gauss points of the tetrahedral cell:

$$\mathbf{T} = \begin{bmatrix} 0.816847572980459 & 0.091576213509771 & 0.091576213509771 \\ 0.091576213509771 & 0.816847572980459 & 0.091576213509771 \\ 0.091576213509771 & 0.091576213509771 & 0.816847572980459 \\ 0.108103018168070 & 0.445948490915965 & 0.445948490915965 \\ 0.445948490915965 & 0.108103018168070 & 0.445948490915965 \\ 0.445948490915965 & 0.445948490915965 & 0.108103018168070 \end{bmatrix} \quad (\text{A.3})$$

as the triangular coordinates, and

$$\mathbf{w} = \begin{bmatrix} 0.109951743655322 \\ 0.109951743655322 \\ 0.109951743655322 \\ 0.223381589678011 \\ 0.223381589678011 \\ 0.223381589678011 \end{bmatrix} \quad (\text{A.4})$$

as the corresponding weights

Acknowledgement

A. Ortiz-Bernardin would like to express his gratitude for the financial support provided by CONICYT-FONDECYT/Iniciación under Grant No. 11110389. J. S. Hale and C. J. Cyron acknowledge the funding provided by CONICYT-FONDECYT/Iniciación under Grant No. 11110389, which made possible a short research stay in Chile. The work of Jack S. Hale is supported by the National Research Fund, Luxembourg, and cofunded under the Marie Curie Actions of the European Commission (FP7-COFUND).

References

- [1] J. C. Simo, R. L. Taylor, K. S. Pister, Variational and projection methods for the volume constraint in finite deformation elasto-plasticity, *Computer Methods in Applied Mechanics and Engineering* 51 (1–3) (1985) 177–208.
- [2] J. C. Simo, F. Armero, Geometrically non-linear enhanced strain mixed methods and the method of incompatible modes, *International Journal for Numerical Methods in Engineering* 33 (7) (1992) 1413–1449.

- [3] T. Sussman, K. J. Bathe, A finite element formulation for nonlinear incompressible elastic and inelastic analysis, *Computers and Structures* 26 (1–2) (1987) 357–409.
- [4] P. Hansbo, M. G. Larson, Discontinuous Galerkin methods for incompressible and nearly incompressible elasticity by Nitsche’s method, *Computer Methods in Applied Mechanics and Engineering* 191 (17–18) (2002) 1895–1908.
- [5] T. P. Wihler, Locking-free DGFEM for elasticity problems in polygons, *IMA Journal of Numerical Analysis* 24 (1) (2004) 45–75.
- [6] R. Liu, M. F. Wheeler, C. N. Dawson, A three-dimensional nodal-based implementation of a family of discontinuous Galerkin methods for elasticity problems, *Computers and Structures* 87 (3–4) (2009) 141–150.
- [7] R. Falk, Nonconforming finite element methods for the equations of linear elasticity, *Mathematics of Computations* 57 (196) (1991) 529–550.
- [8] L.-H. Wang, H. Qi, A locking-free scheme of nonconforming rectangular finite element for the planar elasticity, *Journal of Computational Mathematics* 22 (5) (2004) 641–650.
- [9] S. Chen, G. Ren, S. Mao, Second-order locking-free nonconforming elements for planar linear elasticity, *Journal of Computational and Applied Mathematics* 233 (10) (2010) 2534–2548.
- [10] T. J. R. Hughes, Generalization of selective integration procedures to anisotropic and nonlinear media, *International Journal for Numerical Methods in Engineering* 15 (9) (1980) 1413–1418.

- [11] T. Elguedj, Y. Bazilevs, V. Calo, T. J. R. Hughes, \bar{B} -bar and \bar{F} -bar projection methods for nearly incompressible linear and non-linear elasticity and plasticity using higher-order NURBS elements, *Computer Methods in Applied Mechanics and Engineering* 1 (33–40) (2008) 2667–3172.
- [12] F. Auricchio, L. Beirão da Veiga, C. Lovadina, A. Reali, An analysis of some mixed-enhanced finite element for plane linear elasticity, *Computer Methods in Applied Mechanics and Engineering* 194 (27–29) (2005) 2947–2968.
- [13] C. Lovadina, F. Auricchio, On the enhanced strain technique for elasticity problems, *Computers and Structures* 81 (8–11) (2003) 777–787.
- [14] R. L. Taylor, A mixed-enhanced formulation for tetrahedral finite elements, *International Journal for Numerical Methods in Engineering* 47 (1–3) (2000) 205–227.
- [15] E. Oñate, J. Rojek, R. L. Taylor, O. C. Zienkiewicz, Finite calculus formulation for incompressible solids using linear triangles and tetrahedra, *International Journal for Numerical Methods in Engineering* 59 (11) (2004) 1473–1500.
- [16] M. Cervera, M. Chiumenti, Q. Valverde, C. Agelet de Saracibar, Mixed linear/linear simplicial elements for incompressible elasticity and plasticity, *Computer Methods in Applied Mechanics and Engineering* 192 (49–50) (2003) 5249–5263.
- [17] O. C. Zienkiewicz, J. Rojek, R. L. Taylor, M. Pastor, Triangles and tetrahedra in explicit dynamic codes for solids, *International Journal for Numerical Methods in Engineering* 43 (3) (1998) 565–583.

- [18] E. A. de Souza Neto, F. M. A. Pires, D. R. J. Owen, F-bar-based linear triangles and tetrahedra for finite strain analysis of nearly incompressible solids. Part I: formulation and benchmarking, *International Journal for Numerical Methods in Engineering* 62 (3) (2005) 353–383.
- [19] P. Thoutireddy, J. F. Molinari, E. A. Repetto, M. Ortiz, Tetrahedral composite finite elements, *International Journal for Numerical Methods in Engineering* 53 (6) (2002) 1337–1351.
- [20] Y. Guo, M. Ortiz, T. Belytschko, E. A. Repetto, Triangular composite finite elements, *International Journal for Numerical Methods in Engineering* 47 (1–3) (2000) 287–316.
- [21] J. Bonet, A. J. Burton, A simple average nodal pressure tetrahedral element for incompressible and nearly incompressible dynamic explicit applications, *Communications in Numerical Methods in Engineering* 14 (5) (1998) 437–449.
- [22] C. R. Dohrmann, M. W. Heinstein, J. Jung, S. W. Key, W. R. Witkowski, Node-based uniform strain elements for three-node triangular and four-node tetrahedral meshes, *International Journal for Numerical Methods in Engineering* 47 (9) (2000) 1549–1568.
- [23] J. Bonet, M. Marriot, O. Hassan, An averaged nodal deformation gradient linear tetrahedral element for large strain explicit dynamic applications, *Communications in Numerical Methods in Engineering* 17 (8) (2001) 551–561.
- [24] M. A. Puso, J. Solberg, A stabilized nodally integrated tetrahedral, *International Journal for Numerical Methods in Engineering* 67 (6) (2006) 841–867.

- [25] M. Broccardo, M. Micheloni, P. Krysl, Assumed-deformation gradient finite elements with nodal integration for nearly incompressible large deformation analysis, *International Journal for Numerical Methods in Engineering* 78 (9) (2009) 1113–1134.
- [26] A. Ortiz, M. A. Puso, N. Sukumar, Maximum-entropy meshfree method for compressible and near-incompressible elasticity, *Computer Methods in Applied Mechanics and Engineering* 199 (25–28) (2010) 1859–1871.
- [27] B. P. Lamichhane, Inf-sup stable finite-element pairs based on dual meshes and bases for nearly incompressible elasticity, *IMA Journal of Numerical Analysis* 29 (2) (2009) 404–420.
- [28] B. P. Lamichhane, From the Hu-Washizu formulation to the average nodal strain formulation, *Computer Methods in Applied Mechanics and Engineering* 198 (49–52) (2009) 3957–3961.
- [29] P. Krysl, B. Zhu, Locking-free continuum displacement finite elements with nodal integration, *International Journal for Numerical Methods in Engineering* 76 (7) (2008) 1020–1043.
- [30] G. Castellazzi, P. Krysl, Patch-averaged assumed strain finite elements for stress analysis, *International Journal for Numerical Methods in Engineering* 90 (13) (2012) 1618–1635.
- [31] J. C. Simo, T. J. R. Hughes, On the variational foundations of assumed strain methods, *Journal of Applied Mechanics* 53 (1) (1986) 51–54.
- [32] H. Nguyen-Xuan, G. R. Liu, An edge-based smoothed finite element method

- softened with a bubble function (bES-FEM) for solid mechanics problems, *Computers and Structures* 128 (0) (2013) 14–30.
- [33] F. Brezzi, On the existence, uniqueness and approximation of saddle-point problems arising from Lagrangian multipliers, *RAIRO, Analyse Numérique* 8 (1974) 129–151.
- [34] O. A. Ladyzhenskaya, *The Mathematical Theory of Viscous Incompressible Flows*, Gordon and Breach, London, 1969.
- [35] I. Babuška, The finite element method with Lagrangian multipliers, *Numerische Mathematik* 20 (3) (1973) 179–192.
- [36] J. Dolbow, T. Belytschko, Numerical integration of Galerkin weak form in mesh-free methods, *Computational Mechanics* 23 (3) (1999) 219–230.
- [37] I. Babuška, U. Banerjee, J. E. Osborn, Q. L. Li, Quadrature for meshless methods, *International Journal for Numerical Methods in Engineering* 76 (9) (2008) 1434–1470.
- [38] I. Babuška, U. Banerjee, J. E. Osborn, Q. Zhang, Effect of numerical integration on meshless methods, *Computer Methods in Applied Mechanics and Engineering* 198 (37–40) (2009) 2886–2897.
- [39] J. S. Chen, C. T. Wu, S. Yoon, Y. You, A stabilized conforming nodal integration for Galerkin mesh-free methods, *International Journal for Numerical Methods in Engineering* 50 (2) (2001) 435–466.
- [40] A. Ortiz, M. Puso, N. Sukumar, Maximum-entropy meshfree method for incompressible media problems, *Finite Elements in Analysis and Design* 47 (6) (2011) 572–585.

- [41] Q. Duan, X. Li, H. Zhang, T. Belytschko, Second-order accurate derivatives and integration schemes for meshfree methods, *International Journal for Numerical Methods in Engineering* 92 (4) (2012) 399–424.
- [42] J.-S. Chen, M. Hillman, M. Rüter, An arbitrary order variationally consistent integration for Galerkin meshfree methods, *International Journal for Numerical Methods in Engineering* 95 (5) (2013) 387–418.
- [43] Q. Duan, X. Gao, B. Wang, , X. Li, H. Zhang, T. Belytschko, Y. Shao, Consistent element-free Galerkin method, *International Journal for Numerical Methods in Engineering* 99 (2) (2014) 79–101.
- [44] Q. Duan, X. Gao, B. Wang, X. Li, H. Zhang, A four-point integration scheme with quadratic exactness for three-dimensional element-free Galerkin method based on variationally consistent formulation, *Computer Methods in Applied Mechanics and Engineering* 280 (0) (2014) 84–116.
- [45] C. Wu, W. Hu, Meshfree-enriched simplex elements with strain smoothing for the finite element analysis of compressible and nearly incompressible solids, *Computer Methods in Applied Mechanics and Engineering* 200 (45–46) (2011) 2991–3010.
- [46] D. N. Arnold, F. Brezzi, M. Fortin, A stable finite element for the Stokes equations, *Calcolo* 21 (4) (1984) 337–344.
- [47] N. Sukumar, Construction of polygonal interpolants: a maximum entropy approach, *International Journal for Numerical Methods in Engineering* 61 (12) (2004) 2159–2181.

- [48] M. Arroyo, M. Ortiz, Local maximum-entropy approximation schemes: a seamless bridge between finite elements and meshfree methods, *International Journal for Numerical Methods in Engineering* 65 (13) (2006) 2167–2202.
- [49] N. Sukumar, R. W. Wright, Overview and construction of meshfree basis functions: from moving least squares to entropy approximants, *International Journal for Numerical Methods in Engineering* 70 (2) (2007) 181–205.
- [50] C. J. Cyron, M. Arroyo, M. Ortiz, Smooth, second order, non-negative meshfree approximants selected by maximum entropy, *International Journal for Numerical Methods in Engineering* 79 (13) (2009) 1605–1632.
- [51] J. G. Wang, G. R. Liu, A point interpolation meshless method based on radial basis functions, *International Journal for Numerical Methods in Engineering* 54 (11) (2002) 1623–1648.
- [52] G. R. Liu, *Meshfree Methods: Moving Beyond the Finite Element Method*, 2nd Edition, CRC Press, Boca Raton, FL, 2010.
- [53] F. Greco, N. Sukumar, Derivatives of maximum-entropy basis functions on the boundary: theory and computations, *International Journal for Numerical Methods in Engineering* 94 (12) (2013) 1123–1149.
- [54] G. E. Fasshauer, *Meshfree approximation methods with Matlab*, World Scientific Pub Co Inc, 2007.
- [55] M. D. Buhmann, A new class of radial basis functions with compact support, *Mathematics of Computation* 70 (233) (2000) 307–318.
- [56] T. J. R. Hughes, *The Finite Element Method: Linear Static and Dynamic Finite Element Analysis*, Dover Publications, Inc, Mineola, NY, 2000.

- [57] M. Crouzeix, P.-A. Raviart, Conforming and nonconforming finite element methods for solving the stationary Stokes equations. I., *Rev. Franc. Automat. Inform. Rech. Operat.*, R 7 (3) (1974) 33–76.
- [58] P. Hood, C. Taylor, Navier-stokes equations using mixed interpolations, in: J. T. Oden, O. C. Zienkiewicz, R. H. Gallagher, C. Taylor (Eds.), *Finite Element Methods in Flow Problems*, UAH Press, The University of Alabama in Huntsville, Huntsville, AL, 1974, pp. 121–132.
- [59] S. P. Timoshenko, J. N. Goodier, *Theory of Elasticity*, 3rd Edition, McGraw-Hill, NY, 1970.
- [60] J. C. Simo, S. Rifai, A class of mixed assumed strain methods and the method of incompatible modes, *International Journal for Numerical Methods in Engineering* 29 (8) (1990) 1595–1638.
- [61] P. Hauret, E. Kuhl, M. Ortiz, Diamond elements: a finite element/discrete-mechanics approximation scheme with guaranteed optimal convergence in incompressible elasticity, *International Journal for Numerical Methods in Engineering* 72 (3) (2007) 253–294.
- [62] N. Kikuchi, Remarks on 4CST-elements for incompressible materials, *Computer Methods in Applied Mechanics and Engineering* 37 (1) (1983) 109–123.